Stress and fracture characterization in a shale reservoir, North Texas, using correlation between new seismic attributes and well data

---

A Thesis

Presented to

the Faculty of the Department of Geosciences

University of Houston

In Partial Fulfillment

of the Requirements for the Degree

Master of Science

By

Yves Serge Simon

December 2005

Stress and fracture characterization in a shale reservoir, North Texas, using correlation between new seismic attributes and well data

----
Yves Serge Simon

APPROVED BY:

Dr. Kurt Marfurt, Chairman

Dr. Charlotte Sullivan

Dr. Hua-Wei Zhou

Dr. Heloise Lynn, Lynn Incorporated

Dr. John L. Bear, Dean, College of
Natural Sciences and Mathematics

ACKNOWLEDGEMENTS

For their material and intellectual support, my special thanks to

Dr. Kurt Marfurt (University of Houston),

Mike Ammerman (Devon Energy),

Dr. Heloise Lynn and Dr. Walter Lynn (Lynn Incorporated),

Dr. Charlotte Sullivan (University of Houston), and

Michele Simon (Amerada Hess).

Stress and fracture characterization in a shale reservoir, North Texas, using correlation between new seismic attributes and well data

---

An Abstract of a Thesis

Presented to

the Faculty of the Department of Geosciences

University of Houston

In Partial Fulfillment

of the Requirements for the Degree

Master of Science

By

Yves Serge Simon

December 2005

ABSTRACT

In low primary permeability reservoirs, including tight sand or shale reservoirs, production of oil and gas is highly dependent on natural fractures and / or induced fractures created by high-pressure injection of fluid. The horizontal extent and azimuth of these induced fractures depend on present horizontal stress fields.

The goal of this study is to define the dominant horizontal stress field, as well as, if possible, the relative density and azimuth of vertical natural fractures using new seismic attributes, including azimuthal interval velocity, curvature and inter-azimuth similarity extracted from a 3D wide-azimuth seismic survey acquired in North Texas.

To reach this goal, I use E.U.R. (Estimated Ultimate Recovery) from 122 wells and micro-seismic monitoring of 6 hydrofrac'd wells to test the new seismic attributes with both quantitative (cross correlations) and qualitative (multi-layer attribute maps) techniques.

Only one seismic attribute, the fast interval velocity, has a significant (inverse) numerical cross-correlation with well production. But visual examination of multi-layer maps shows a correlation between creation of hydrofrac-induced fractures orthogonal to the regional main horizontal stress field and the azimuth of fast interval velocity when the velocity anisotropy is above a threshold of ~500 ft/s (150 m/s). I verified successfully this result numerically using E.U.R. of wells drilled after the 3D seismic acquisition.

In addition, the following observations may help those attempting a similar workflow:

- Stress fields are modified by hydrofracs; therefore, wells hydrofrac'd before the 3D seismic acquisition should not be used to calibrate seismic attributes such as azimuthal interval velocity;

- Inter-azimuth coherence images have disappointingly poor correlation with velocity anisotropy;

- In the south part of the survey, there is a visual correlation between the azimuth of the fast interval velocity and structural deformation imaged by volumetric curvature.

Table of Contents

Table of Abbreviations

T: Reflector at the top of the reservoir
M: Phantom horizon in the middle of the reservoir
B: Reflector at the bottom of the reservoir

Vf, or Vfast: Fastest azimuthal interval velocity
Vs, or Vslow: Slowest azimuthal interval velocity
Vf – Vs : (Fast – Slow) interval velocity
AzimVf: Azimuth of fastest interval velocity

Kmax: Maximum curvature
Kmin: Minimum curvature
K+, or Kpos: Most positive curvature (convex)
K-, or Kneg: Most negative curvature (concave)

Nears, or SimNears: Similarity between SW-NE and SE-NW volumes, near-offset data (0° to 20° at reservoir depth). 0 means a perfect similarity, 1 a total dissimilarity.
Fars, or SimFars: Similarity between SW-NE and SE-NW volumes, far-offset data (20° to ~45° at reservoir depth)\

E.U.R.: Estimated Ultimate Recovery. Projected total gas production of a well.
ρ, or N.C.C.: Normalized Cross-Correlation, values from –1 to +1.

1. INTRODUCTION

In low primary permeability reservoirs, including carbonates, tight sands and unconventional or shale reservoirs, production of oil and gas is highly dependent on fractures. If these fractures are rare, very thin or filled with non-permeable material such as calcite, they must be enlarged by injection of high-pressure fluid. These high-pressure injections can create new fractures; their horizontal extent and azimuth depend on present horizontal stress fields.

The task of the geophysicist in this kind of reservoir is to improve production by assessment of natural fracture density and azimuth, as well as horizontal stress strength and azimuth. The vertical fractures may be aligned with present stress; but often, the stress field has changed since their creation. Therefore, one of the geophysical challenges is to differentiate the effect of horizontal stress and natural fractures on seismic response.

In this study, my goal is to describe current horizontal stresses and vertical fractures in a North Texas reservoir using new, specific seismic attributes. To define the geological significance of these new attributes, I cross-correlated them against well data and against each other.

2. GEOLOGICAL BACKGROUND

2.1. Fort Worth Basin: Origin and Structure

The Fort Worth basin is a Paleozoic foreland basin, formed in the Early to Middle Pennsylvanian Period, as a result of the Ouachita orogeny (Thompson, 1982). Figure 1 shows the major tectonic elements of the basin, which covers about 20,300 square miles (52,000 sq. km) in North Central Texas. The wedge of Paleozoic sediments reaches a maximum thickness of approximately 12,000 ft (3660m) in the northeast of the basin, adjacent to the Munster Arch, and becomes thinner in the broad structural high of the Bend Flexure and the Concho Platform towards the west; the Llano uplift bounds the basin to the south. A thin veneer of Cretaceous rocks covers the Paleozoic sediments in the eastern part of the basin. Stratigraphic relationships and burial-history reconstructions suggest that a significant thickness of upper Pennsylvanian and possibly Permian strata were eroded prior to Cretaceous deposition (Montgomery *et al*, 2005). Nonetheless, the most prolific shale gas fields are located in the present-day deepest portion of the basin.

Most models explain the Ouachita Thrust Belt by a continent-continent collision during the formation of Pangea (Walper, 1982). The Ouachita Thrust Belt is a classic thin-skinned fold and thrust belt, with thrust sheets either buttressed by pre-existing positive areas on the craton (such as the Llano Uplift) or riding over pre-existing embayments. The Fort Worth basin was produced by downwarping of a pre-existing carbonate platform (Ellenburger) adjacent to the westward-advancing thrust front (Thompson, 1982). Continued subsidence and infill of the basin from the uplifted highlands of the thrust front resulted in westward progression of the deposition center with time. The tectonic forces (SE-NW compression) that produced the Ouachita thrust belt exerted a strong control on the structures found in the Fort Worth basin, as well as on its depositional history.

Structure within the basin is complex and varied. Thrust-fold structures exist in the eastern part of the basin (Walper, 1982). The Red River / Electra Arch is a series of discontinuous fault blocks that strike west-northwest at the northern edge of the basin (Flawn *et al*, 1961). The northwest-striking Muenster Arch was uplifted in response to compressional stresses from the Ouachita during late Mississippian to Late Pennsylvanian time (Thompson, 1982). The southwest flank of the Muenster Arch is bounded by a series of down-to-the-southwest faults with displacement estimated at 5000 ft (1524m) (Flawn *et al*., 1961). Intra-basin faults that formed in response to subsidence show normal displacement. In the central and southern parts of the basin, faults trend north-south or northeast-southwest coinciding with major faults of the Llano uplift and subparallel to the Ouachita thrust front.

The Mineral Wells fault is a major northeast-southwest striking feature extending for more than 65 miles (100 km) through the heart of the shale producing areas, and does not appear directly related to either the Red River-Muenster arches or the Ouachita front (Montgomery *et al*, 2005). In the northern part of the basin, many faults within the producing gas fields show this northeast-southwest trend.

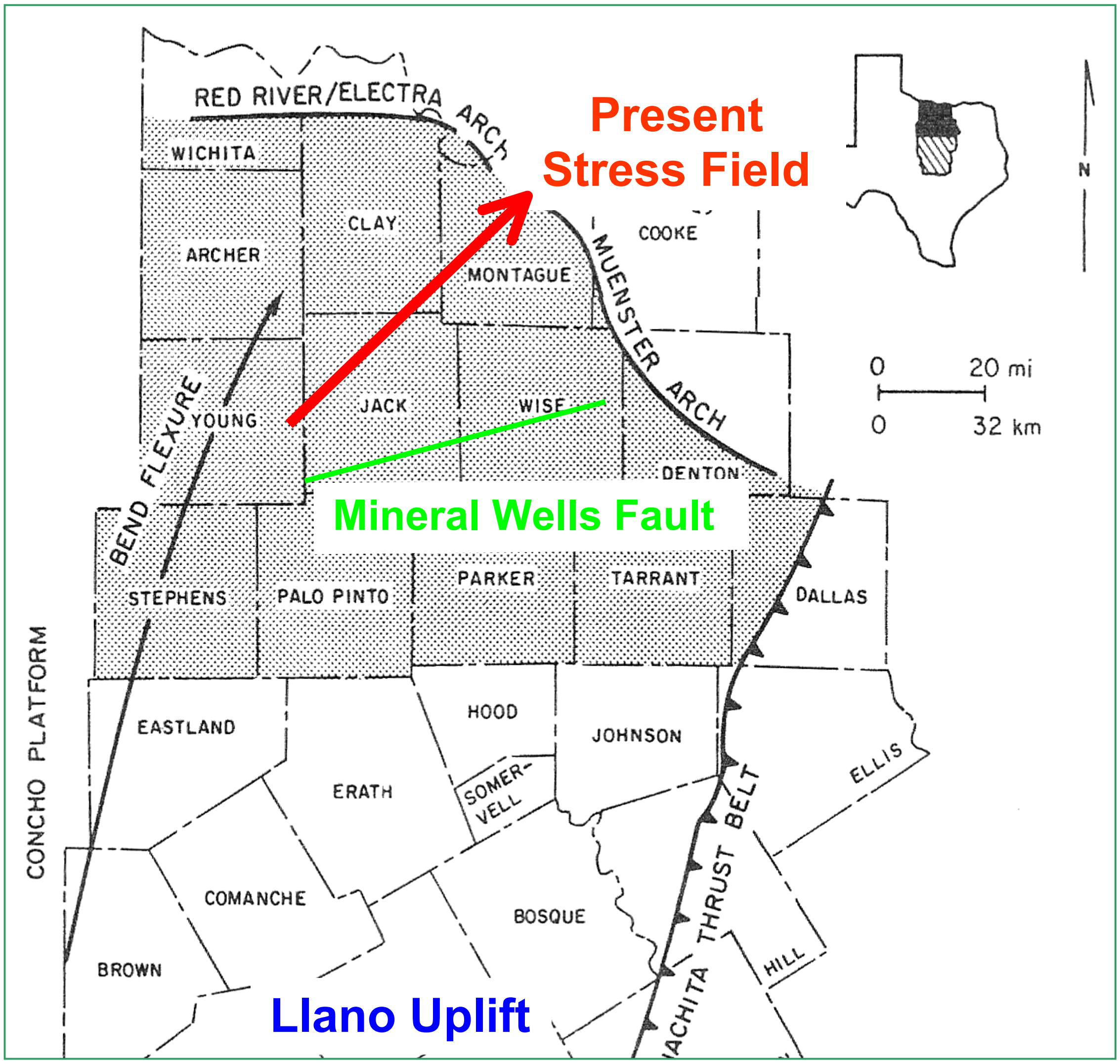

Figure 1: Map showing major geological features of North Texas (After Thompson, 1982)

2.2. Stratigraphy and Lithology

Figure 2 shows the generalized stratigraphic column of the Fort Worth basin. The Paleozoic section can be broken into three main intervals based on tectonic history (Montgomery *et al*, 2005):

- Stable carbonate platform strata (Cambro-Ordovician),

- Shallow- and deep- marine, subsidence-related strata (Middle and Upper Mississippian)
- Terrigenous basin-infilling strata derived mainly from the Ouachita highlands (Pennsylvanian).

The Mississipian reservoir, deposited during the early phase period of basin subsidence, is a highly organic, radioactive black shale that overlies the Ordovician Viola-Simpson Group in the area of this study. Westwards, the Viola-Simpson is absent due to erosion, and the shale reservoir directly overlies the Ordovician Ellenburger limestone.

Gross thickness of the shale reservoir in the basin ranges from 50-1000 ft (9-305m). In the northeast part of the basin, it contains a limestone wedge (the Forestburg) that thins away from the Muenster Arch. In the most-drilled (best-known) areas of the basin, including the area of this study, the shale reservoir is about 300-600 ft (90-180m) thick and is subdivided into an upper and a lower member, separated by the thin (less than 60 m) Forestburg limestone. The limestone portion of the shale reservoir thins rapidly to the south and west. In this study, only the lower shale reservoir is considered. Lithologically, the reservoir is made up of siliceous shale, limestone and dolomite. It is rich in silica (35-50% by volume) and poor in clay (< 35 %; Montgomery *et al*., 2005). Reservoir characteristics include porosity averaging 6%, permeability in the nanodarcies, and 75% gas saturation. Organic content of the shale reservoir varies with lithology and thermal maturity. TOC (Total

Organic Carbon, by weight) from reservoir core samples ranges from 3 to 7% (Lancaster *et al.*, 1992), and from exposed outcrop samples, from 11 to 13% (Montgomery *et al.*, 2005). Laboratory maturation studies suggest that original TOC values were in the range of 5 to 12% (Montgomery *et al.*, 2005).

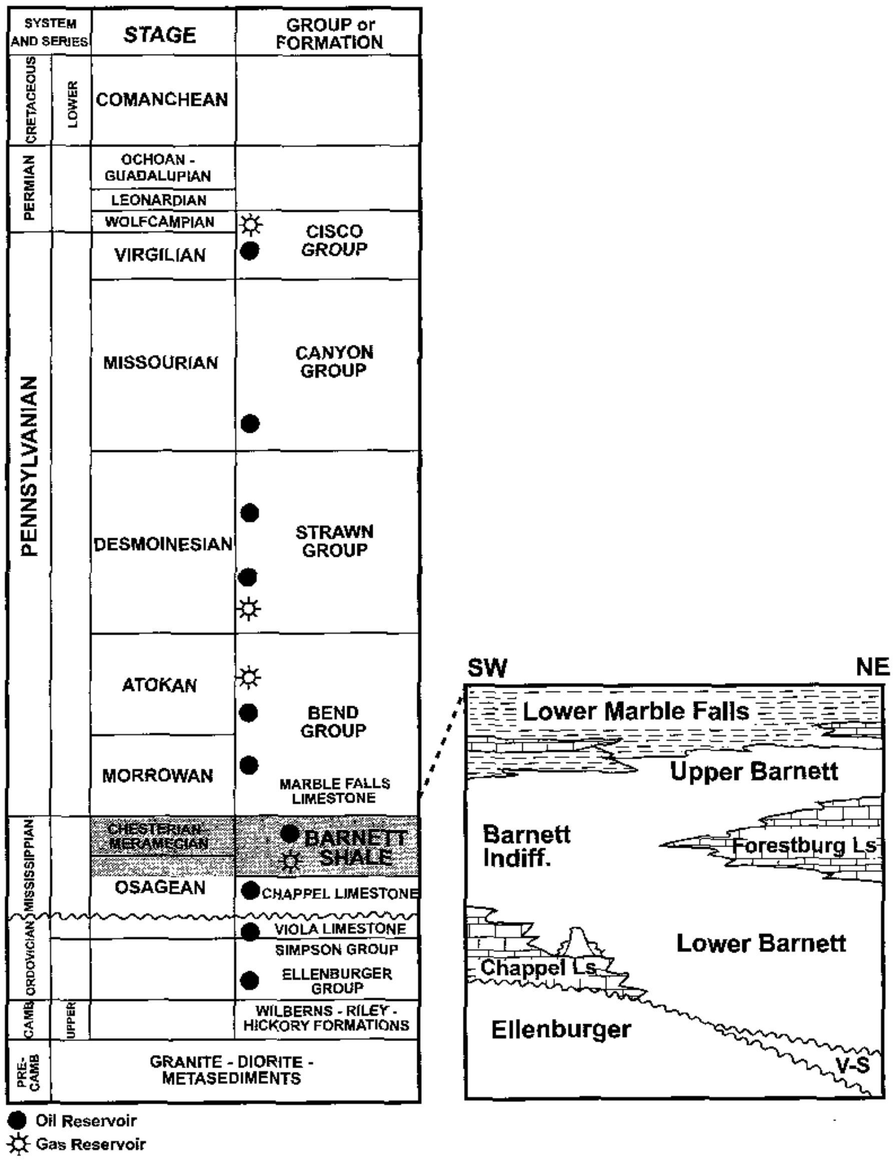

Figure 2: Generalized stratigraphic column and detail of Mississipian strata (From Pollastro, 2003)

2.3. Area of the study

Figure 3 is a time map of the bottom reflector of the reservoir. Irregularly shaped, this field covers approximately 60 km^2. The depth to the bottom of the shale reservoir in this area varies from 2250 to 2550 m, equivalent to 1.2 to 1.35s (two-way traveltime). It is dipping towards the northeast, but the slope is very gentle, around 2%. The thickness of the shale reservoir varies from 75 to 100 meters, or 60 to 80 ms (two-way traveltime; Figure 4).

A southwest-northeast trending fault crosses the field. This fault is oriented parallel to the main regional current stress field, as indicated by the World Stress Map (Heidelberg Academy of Sciences, 1999). Examination of seismic sections and time structure maps at different levels show that this fault is nearly vertical, but has a small normal dip slip overprint.

It also appears that the fault has had some strike-slip motion, as evidenced by change in vertical displacement (throw) along the fault: the throw becomes smaller towards the NE (Figure 3). There is no published information on the slip of this fault, nor the Mineral Wells fault, which trends in the same direction. However, the azimuth of the fast interval velocity (Figure 5) provides some clues to the sense of movement. Knowing that tensile fractures are parallel to strike-slip fault plane on the side going away from the closest tip, but orthogonal to the fault plane on the other side (Bourne *et al*, 2000), I conclude that the main fault in our survey is probably right-lateral.

Examination of the velocity field (Figure 5) shows that the changes in the present stress field and natural fractures are restricted to less than 600 m laterally from the fault plane.

Most of the 122 control wells used in this study lie outside this area: the operator wanted to avoid loss of pressure during hydrofracs.

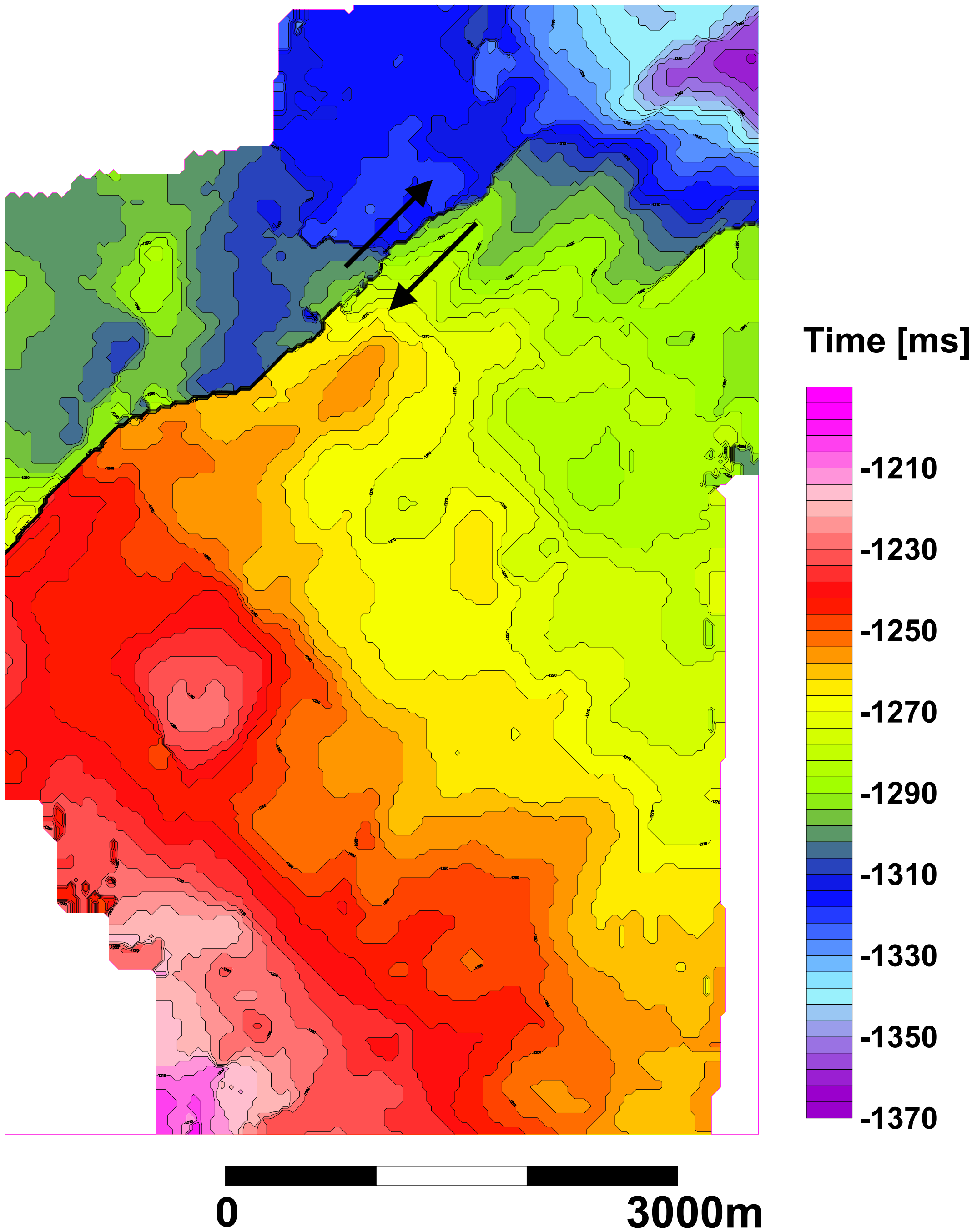

Figure 3: Time map of the bottom of the reservoir (4ms intervals)
Reservoir dips towards NE. The main strike-slip normal fault trends SW-NE

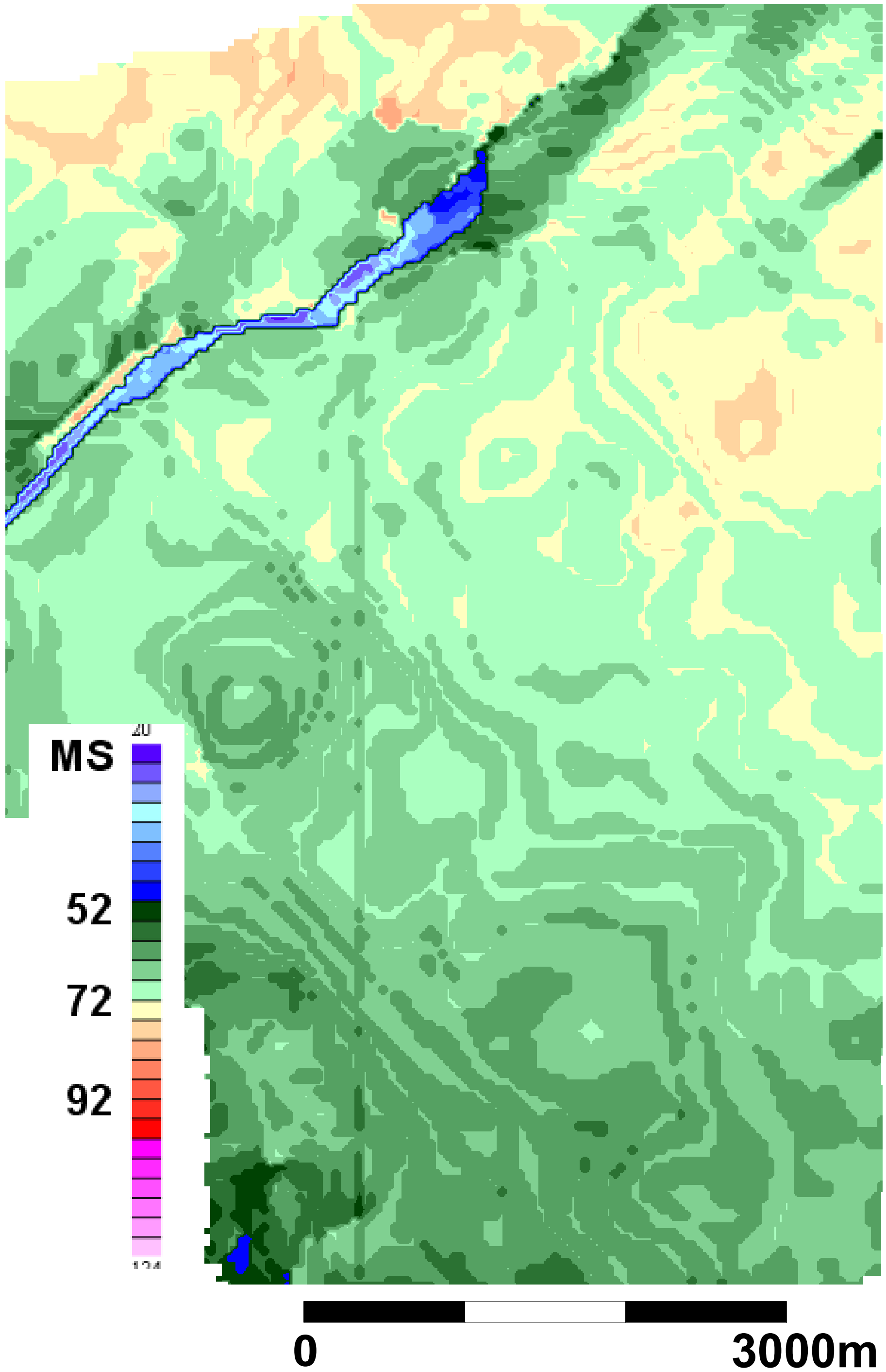

Figure 4: Isochron map of the reservoir (4ms intervals)
The reservoir is slightly thicker towards the NE; the main fault does not define areas of different thickness, showing that the vertical displacement happened after reservoir formation.

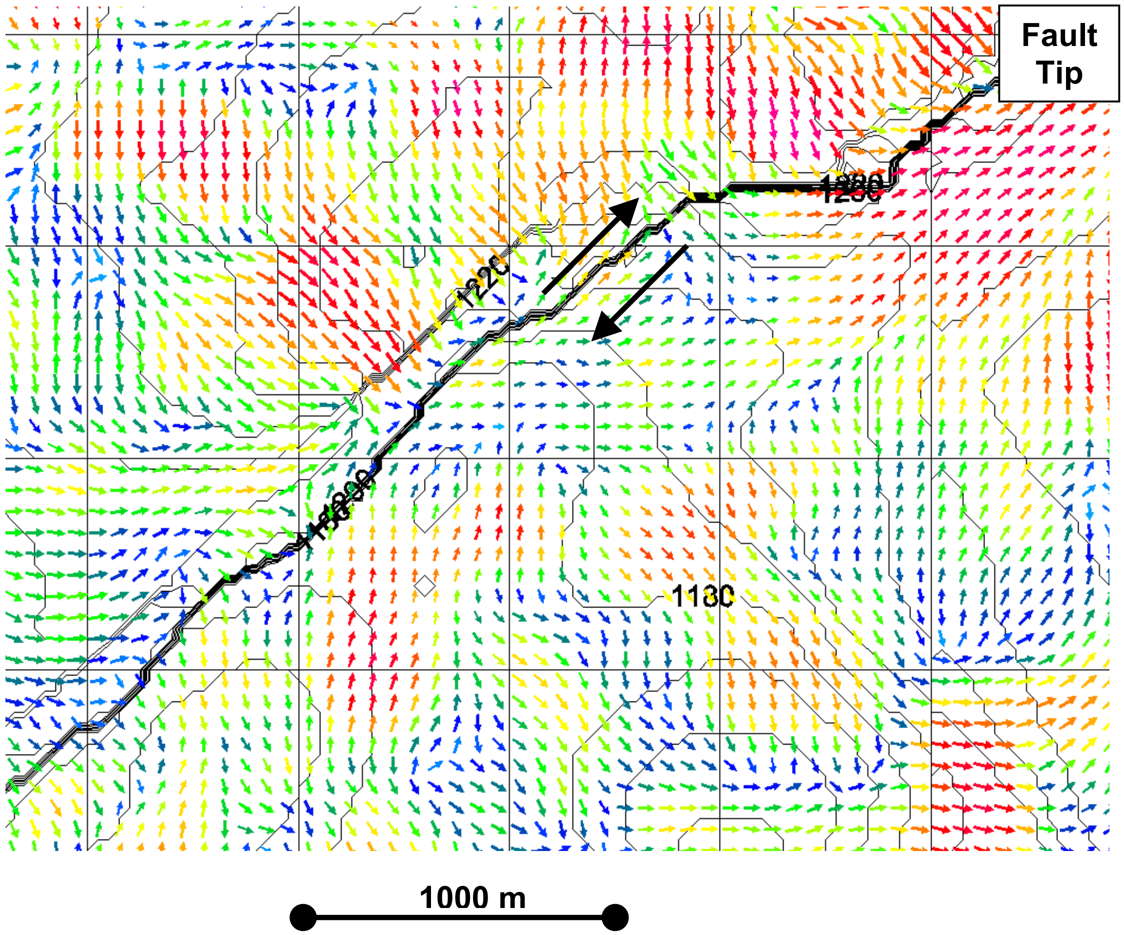

Figure 5: Time contours of the top of the reservoir (4ms contour interval) and azimuthal interval velocity icons. The azimuthal change in the velocity field around the fault is consistent with right-lateral strike-slip motion.

3. DATA FROM WELLS

3.1. Standard well logs

Many density, gamma ray and resistivity logs are available, but only three have P- and S- sonic logs (Figure 6). Exhaustive studies of these logs by fellow geologists and geophysicists have already demonstrated that they are not correlated to gas production, and that lithology is fairly constant in this shale reservoir.

Nevertheless, to better understand the reservoir, I selected a few wells to examine their logs: the three wells with sonic logs (Figures 7 and 8), two wells with a very low E.U.R., and two wells with a very high E.U.R..

Typical reservoir log response includes a high gamma ray: 100 to 200 API units, with thin streaks up to 300 API. The density logs of the reservoir show values between 2.45 and 2.6 g/cc. The P- sonic shows a velocity of 12,000 to 12,500 ft/s (3,650 to 3810 m/s). P- and S- sonics show increased traveltime compared to surrounding carbonates. The ratio Vp/Vs, 1.60 to 1.65, is very low for the shale interval.

The shale reservoir contains a few very thin limestone stringers; the limestone below the reservoir is very fast and dense while above the reservoir, I see many interbedded shale / carbonate layers.

Figure 9 shows that there is no correlation between E.U.R., density and gamma ray for the seven selected wells.

The P- sonic velocity (~12250 ft/s) is lower than the average interval velocity [Vfast - ((Vfast-Vslow) / 2)] calculated from the surface seismic, which is approximately ~15,000 ft/s. This is probably due to usage of a 100 ms sliding vertical window to calculate the interval velocity from the RMS velocity.

The interval velocity values extracted from the middle of the shale reservoir include 20 to 40 % of high velocity limestone, located above and below the reservoir.

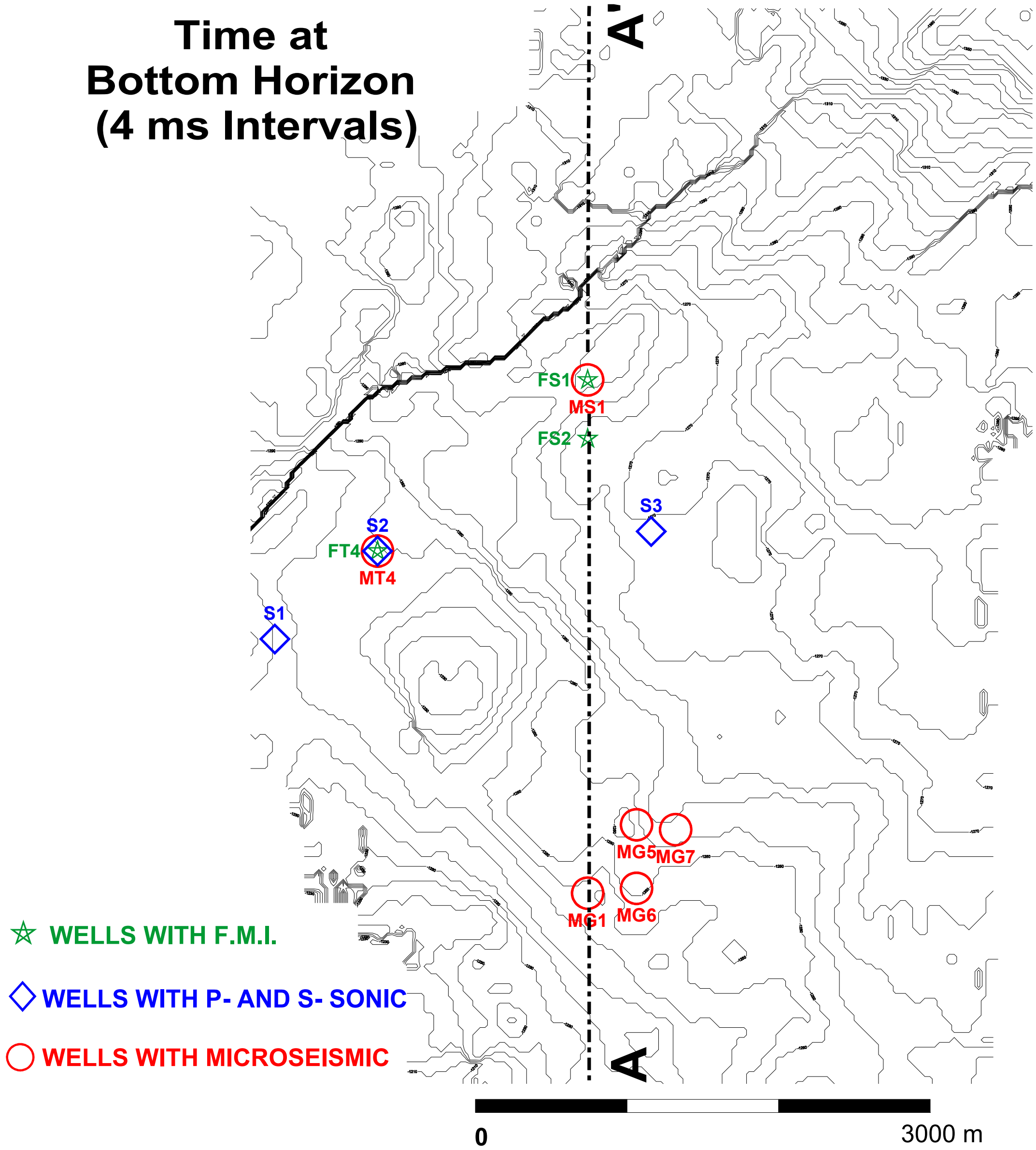

Figure 6: Three wells with FMI logs, three wells with sonic logs, and six wells with micro-seismic measurements during hydrofrac are available.

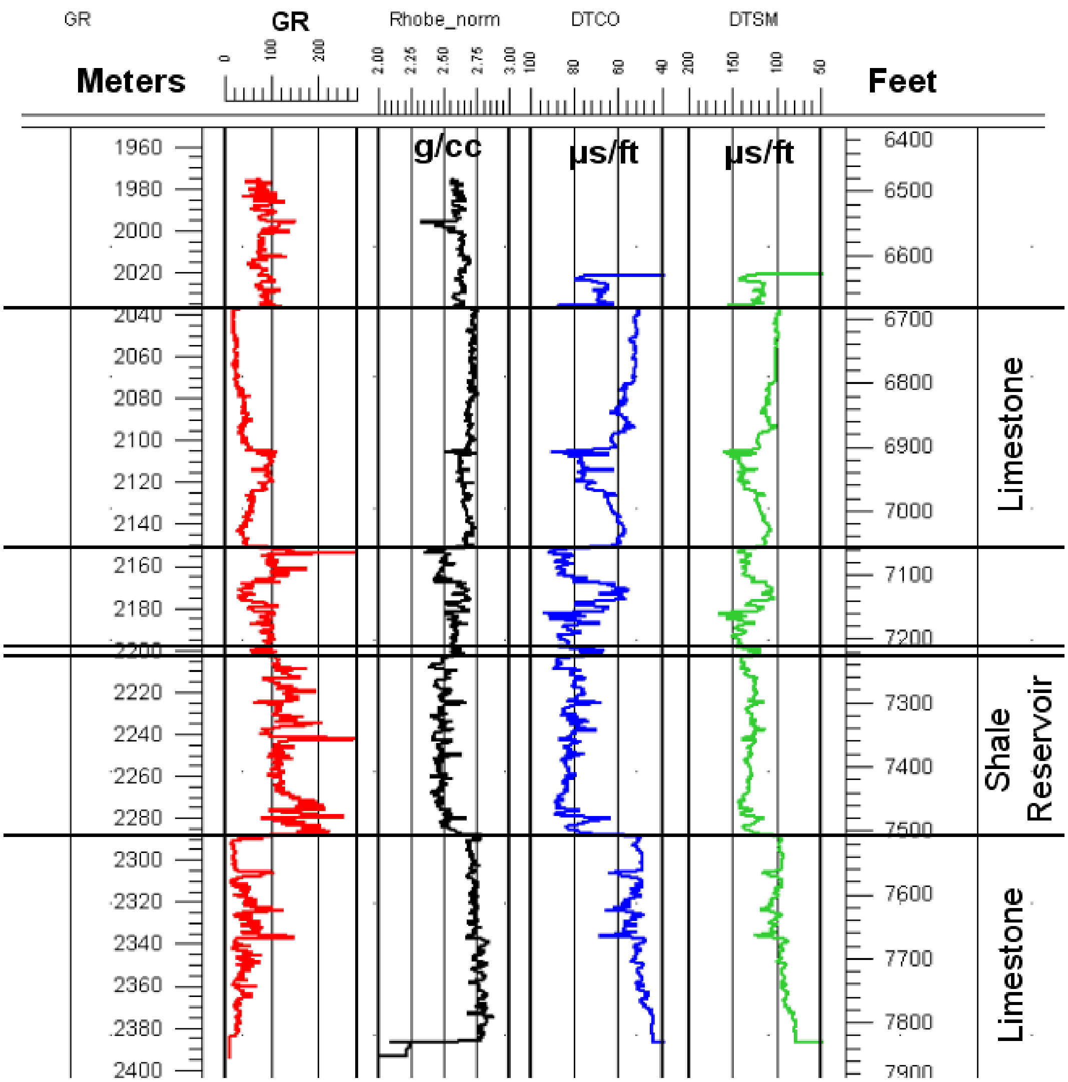

Figure 7: Gamma Ray, Density, P-sonic and S-sonic logs of S2/FT4/MT4. The reservoir is 85 m thick here. The bottom of the reservoir is easier to define than the top, which is made of interbedded layers of shale and limestone.

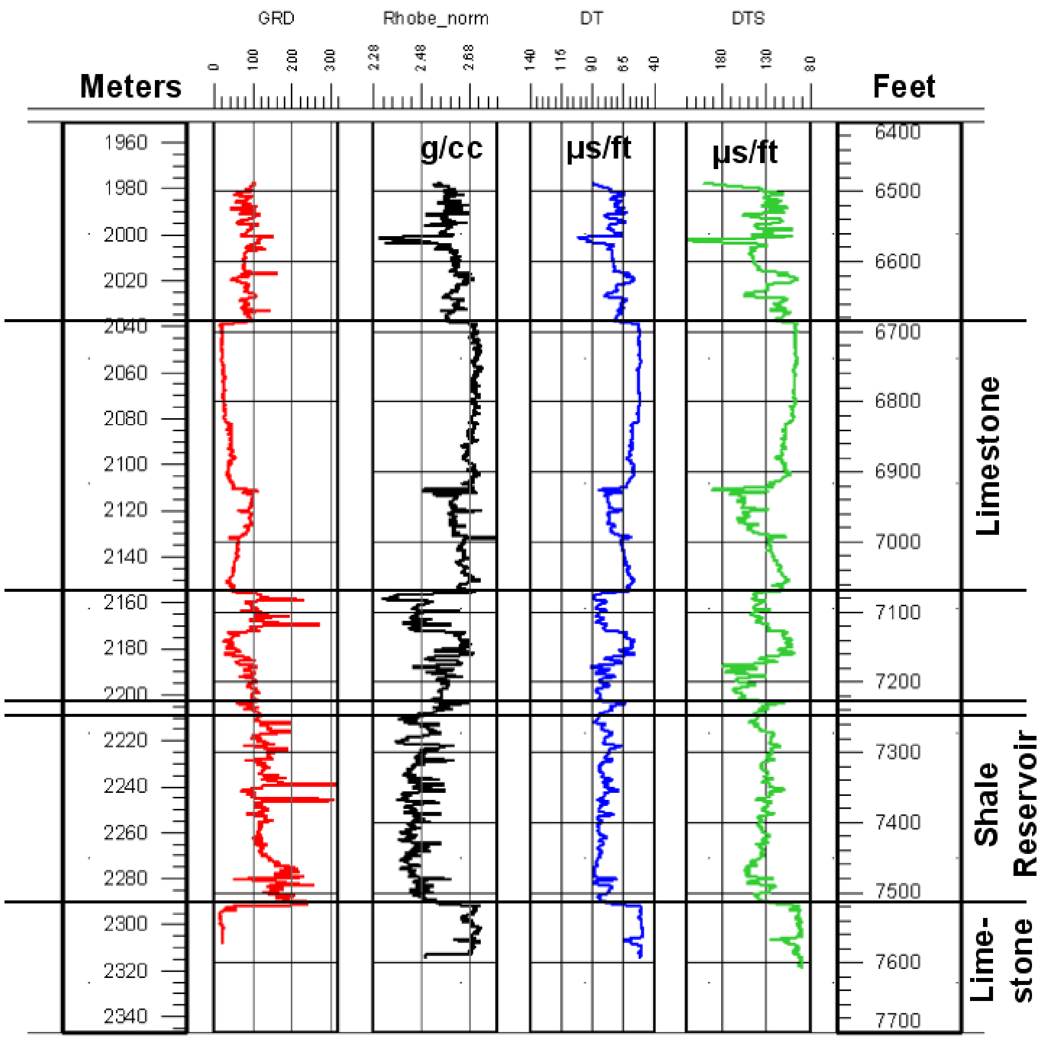

Figure 8: Gamma Ray, Density, P-sonic and S-sonic logs of well S1. The reservoir is 80 meters thick here. The bottom of the reservoir is easier to define than the top, which is made of interbedded layers of shale and limestone.

Wells	Gamma Ray	Density [g/cc]	Vp [ft/s]	Vs [ft/s]	Vp / Vs	E.U.R.
S1	139.72	2.47	12094	7590	1.59	53
S2	129.08	2.49	12503	7735	1.62	36
S3	144.42	2.49	12627	7755	1.63	30
Low1	138.47	2.49	x	x	x	1
Low2	128.17	2.5	x	x	x	3
High1	158.08	2.49	x	x	x	48
High2	127.99	2.48	x	x	x	42

Figure 9: Average log values within the shale reservoir for seven wells, and the E.U.R. for these wells.

3.2. Image logs

Three image logs are available (Figures 6, 9 & 10). These images show that natural fractures are rare, thin, and are nearly always filled with calcite. These natural, pre-drilling fractures are mainly oriented ESE-WNW (N60W), sub-parallel to the Muenster Arch. In contrast, drilling-induced fractures are oriented SW-NE. The variation in azimuth between natural and induced fractures is explained by a change of stress direction during geological time. The present maximum horizontal stress field is SW-NE oriented, but when fractures were created, the maximum horizontal stress direction was SE-NW.

These image logs allow estimation of the maximum horizontal stress azimuth and natural fractures azimuth around the borehole, and they serve to define natural fractures; however, they can image only a few feet outside the borehole. Therefore, these image logs are less useful than microseismic experiments to test seismic attributes.

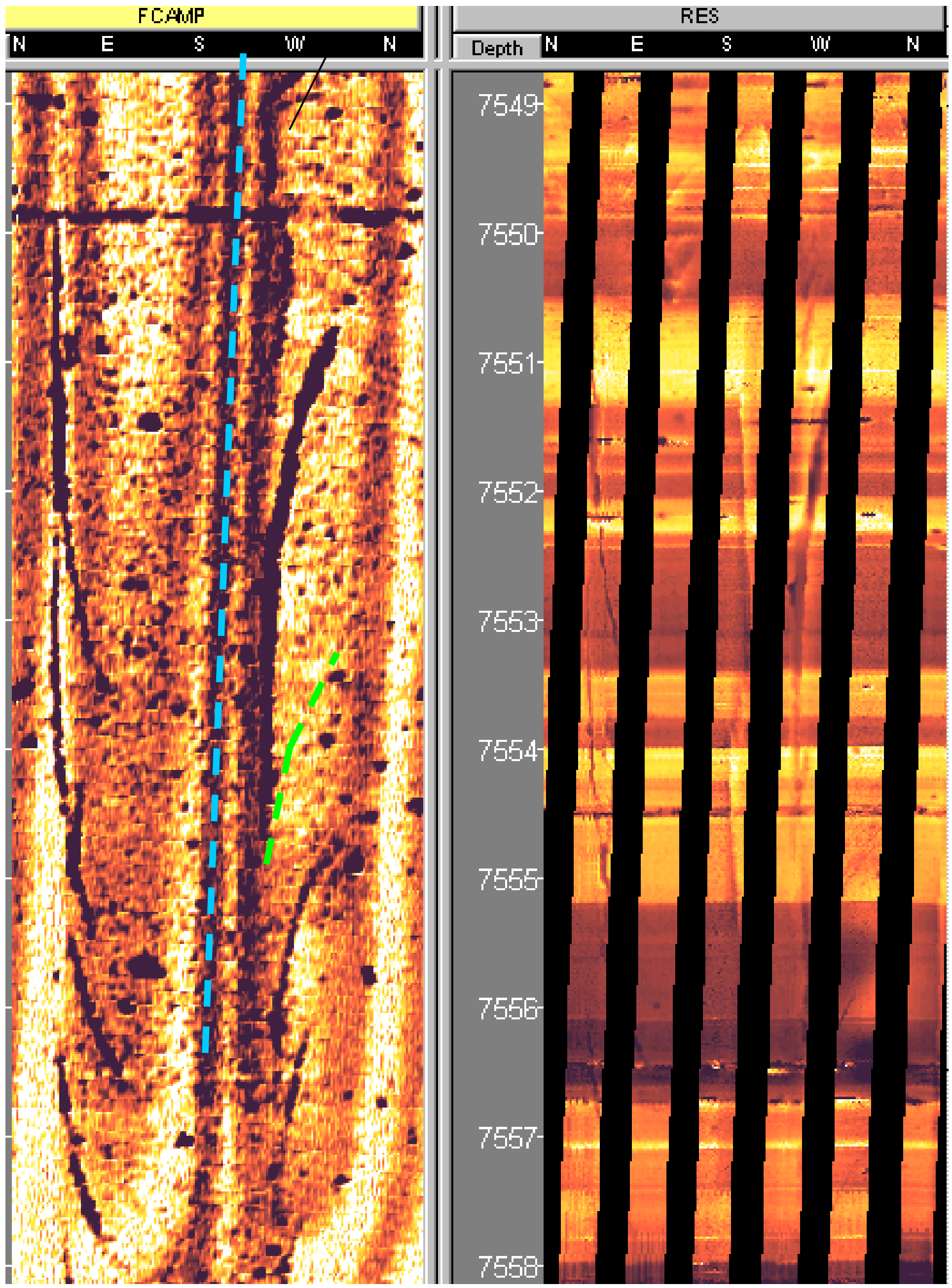

Figure 10: Acoustic and Resistivity images displaying the presence of drilling induced vertical hydraulic fractures (blue dashed lines) and petal natural fractures (green dashed lines). From Baker-Atlas.

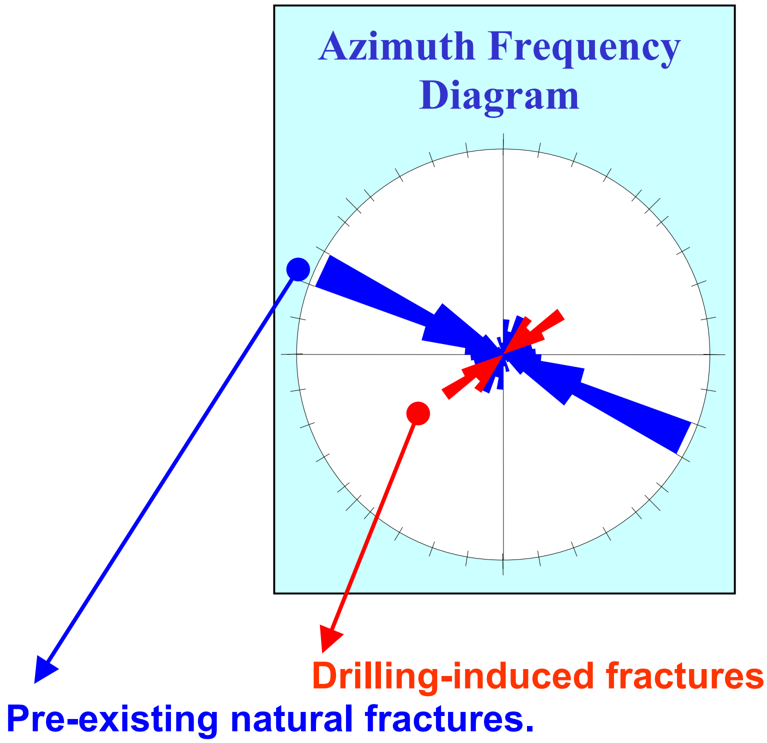

Figure 11: Natural (pre-existing) and induced (by the drilling) fracture azimuth, as seen on resistivity imaging logs. Induced fractures indicates azimuth of main present stress field.

3.3. Micro-seismic measurements

Pinnacle Technology monitored acoustic signals induced by hydraulic fracturing (hydrofracs) of six wells (Figure 6). They used vertical arrays of five to twelve 3-component geophones installed in adjacent well(s) to record the seismic events induced by the hydrofracs. Using triangulation and the difference of arrival time and polarization between P-waves and S-waves and polarization, they located each event. Then, they mapped the induced fractures, taking into account the location and time of occurrence of these events.

The short travelpaths, their high frequency content (maximum amplitude centered on approximately 550 Hz) and the absence of overburden effects resulted in very detailed maps of these induced fractures. We can cautiously use these results to calibrate our seismic attributes. Only micro-seismic records made after the 3D seismic acquisition are useful to calibrate the surface seismic data, since we expect the hydrofracs to modify the stress field in the reservoir, and hence the reservoir's seismic response. Pinnacle Technology, taking into account the timing of the noise events, was able to reconstruct the induced fractures as they propagated (Figure 12).

Surface and down-hole tilt measurements, as well as micro-seismic measurements made during hydrofracs in this field and in similar fields in the area, show that gas recovery is correlated with the creation of a wide inter-connected fracture network; the conventional half-length of induced fracture seems to be irrelevant here (Fisher *et al*, 2003). I will use the fracture maps to calibrate our seismic attributes.

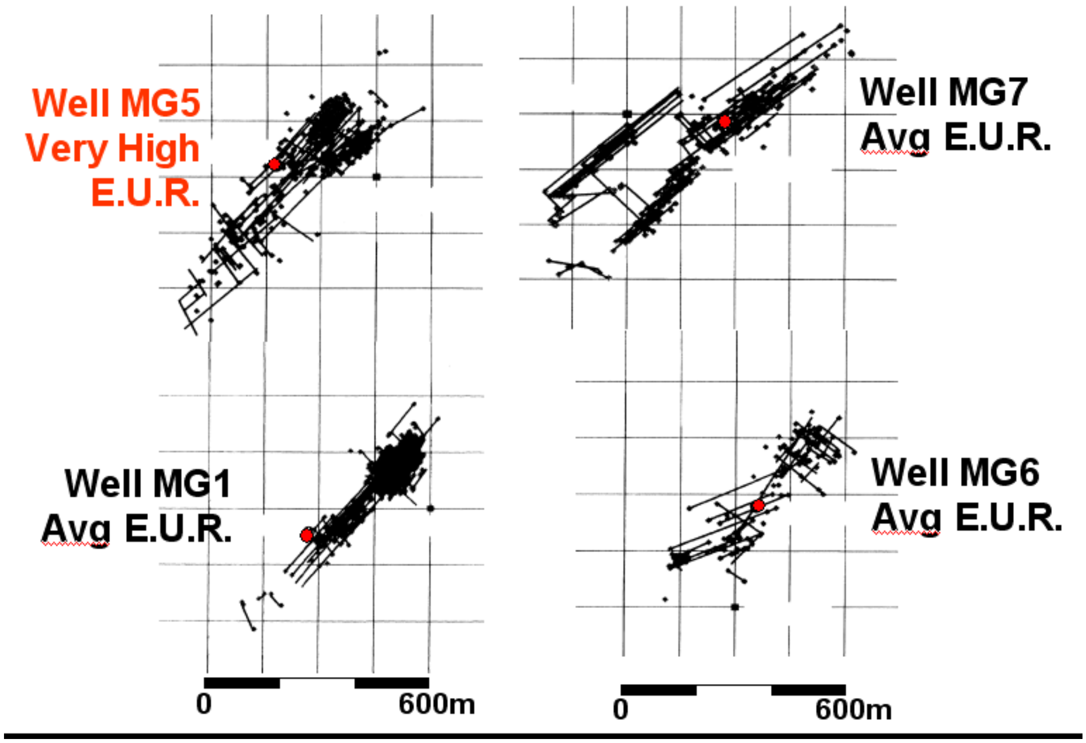

Figure 12: Results of micro-seismic study suggest that E.U.R. depends on creation (by hydrofracs) of large network of multi-azimuth vertical fractures (well MG5). Most induced fractures are oriented SW-NE. Red dots indicate injection wells; black dots indicate location of micro-seismic events due to hydrofracs, lines are interpreted induced fractures. (Modified from Pinnacle Technology)

3.4. Production statistics

Gas production is primarily dependent on artificially-induced fractures, necessary to allow the transfer of gas to the wells. These artificial fractures form parallel to the maximum horizontal stress, and thin, open existing natural fractures (which are rare in the survey) are enlarged. Lab tests to determine if the cemented, natural calcite-filled fractures constitute planes of weakness have not yet been performed; we do not know yet if these cemented fractures might promote creation of larger, open fractures along them.

As gas production is dependent on horizontal stress and possibly on natural fractures, I will use production data to evaluate the seismic attributes in this reservoir.

Engineers and geologists working on this field believe that Estimated Ultimate Recovery (E.U.R.) are the most relevant production data, because this parameter is not sensitive to short-term production variation due to differing completion techniques. They provided these numbers to test the seismic data.

Microseismic measurements and image logs interpretation, in this and adjacent similar fields, show that most induced fractures (by hydrofracs) are oriented SW-NE. But the best gas producers also have many induced orthogonal fractures. These SE-NW fractures link the SW-NE fractures, and this network of multi-azimuth hydrofrac-induced fractures reach a large volume of the reservoir.

The 122 wells used in this study are shown in Figures 13 and 14. Sixty of these wells were drilled and hydorfrac'd before the 3D seismic acquisition, while sixty-two were drilled later. Figure 15 shows a crossplot between the first month's production and two, three and twelve months' production. The correlation is excellent ($R^2 > 0.86$), showing that one-year production can reliably be predicted from only one month of production, and gives us confidence in the validity of Estimated Ultimate Recovery (E.U.R.)

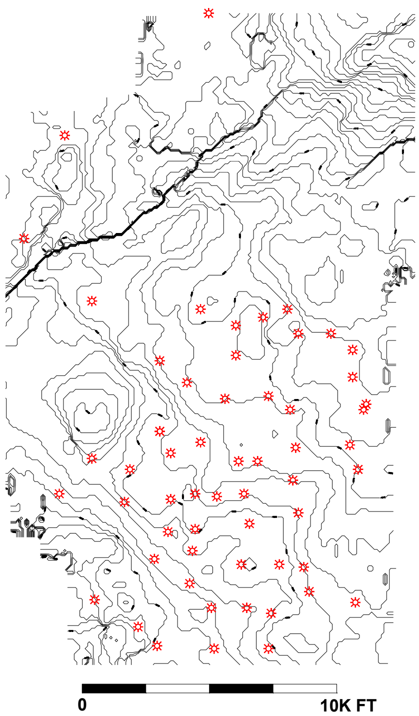

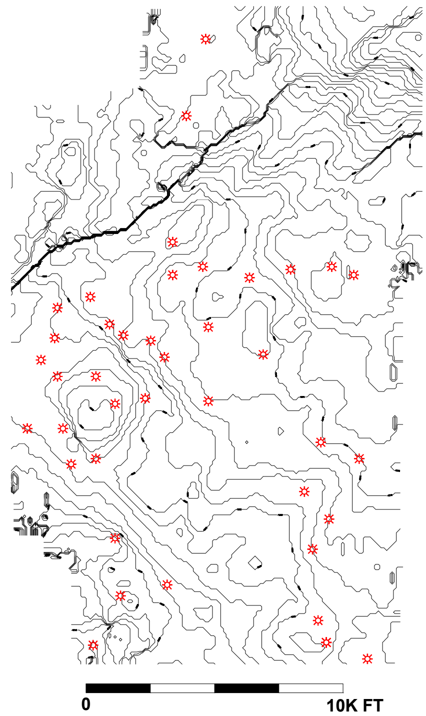

Figures 13 and 14: Red symbols indicate wells drilled and hydrofrac'd before (left) or after (right) the 3D wide-azimuth seismic acquisition.

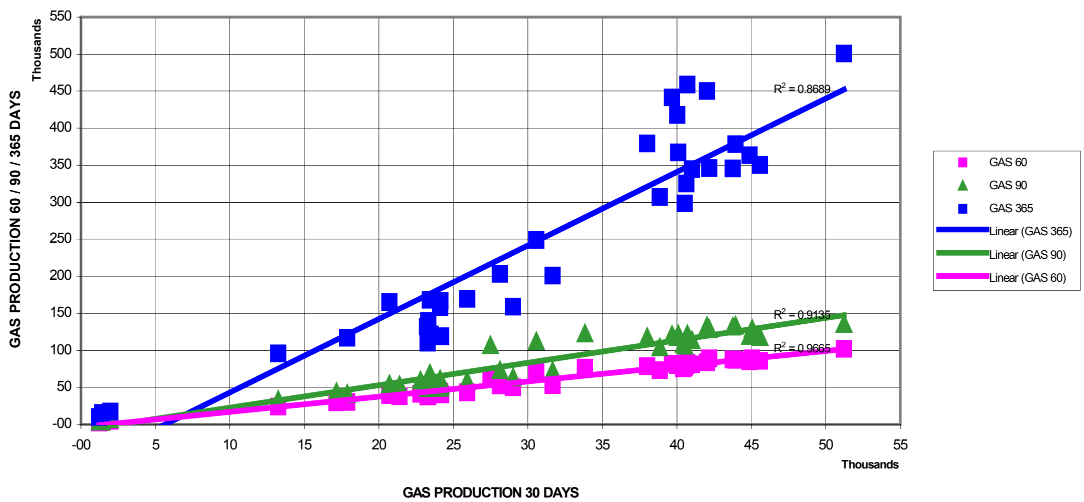

Figure 15: Wells located south of main fault. 30-day gas production (x-axis) against 60-day (pink), 90-day (green) and 365-day (blue) gas production (y-axis). There are excellent linear correlations between these values: R^2= 0.96, 0.91 and 0.87.

4. SEISMIC ATTRIBUTES

A 3D wide-azimuth seismic survey covering 60 km² was acquired in North Texas during the year 2001. Axis Geophysical and Western-Geco processed the data. The post-stack migrated volume is of very high quality, with an average of 109 fold at the target depth. On seismic sections (e.g. Figure 16), the horizon (B) that defines the bottom of the shale reservoir is a strong-amplitude peak, and is easy to map. The top of the reservoir, less easily defined, is composed of a succession of thin (~20 ft / 6 m) limestone / shale beds. For this study, we are using a peak reflector (T, shale above limestone) as the upper limit of the reservoir. The surface seismic velocity of our shale reservoir (~4650 m/s) is higher than that of the overlying limestone / shale intervals (~4200 m/s), and lower than the underlying limestone interval (~6050 m/s).

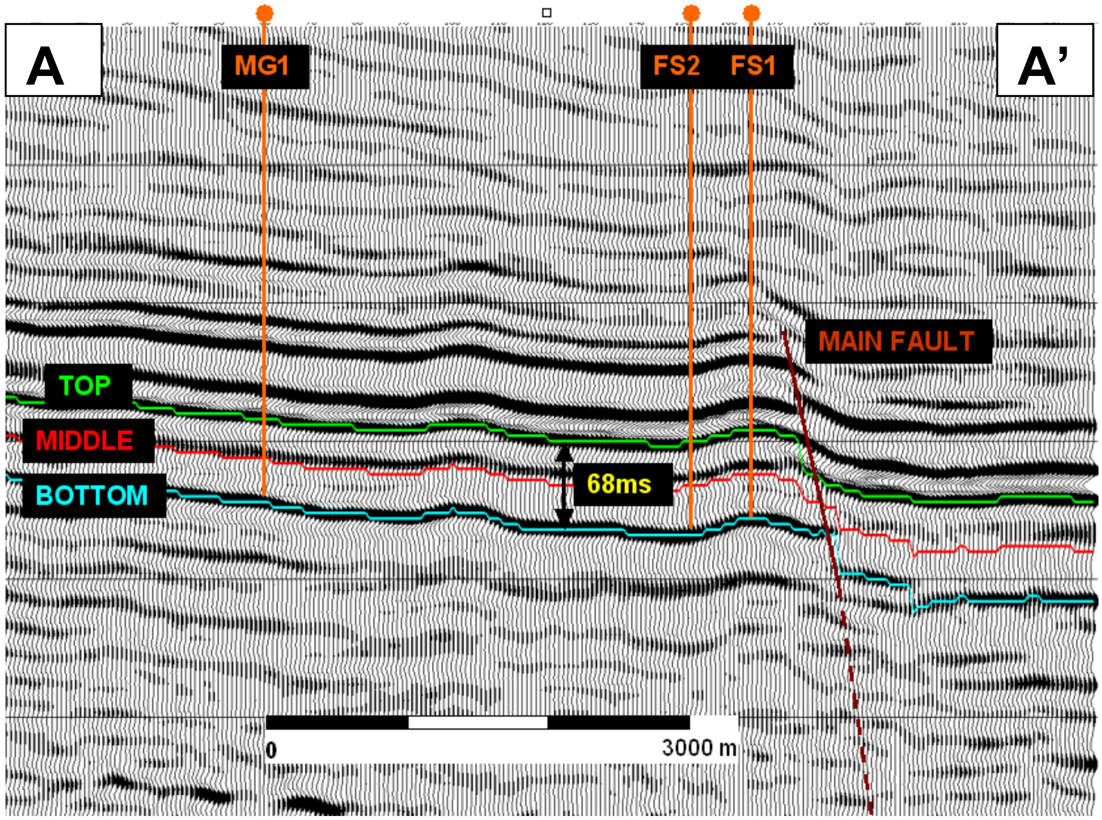

Figure 16: This south-north seismic shows the reservoir. Location: see A-A' on Figure 6. The middle horizon is the phantom horizon used to extract values and make maps of azimuthal interval velocity attributes.

4.1. Azimuthal interval velocity

The processing, done by Axis Geophysical, is based on Jenner's (2001) PhD thesis. After pre-processing, NMO and AGC correction, the traveltime of each source-receiver record is estimated by an Event Alignment Procedure (EAP; Figure 17). Within each CMP gather, the central trace of a 3D window (defined by both time and lateral windows) is cross-correlated with a pilot trace made by stacking of all the traces in the window. An iterative process allows narrowing the vertical and horizontal windows. At the end of the process, a time shift is assigned to each trace of each source-receiver couple.

Grechka and Tsvankin (1998, 1999) defined azimuthally-dependent NMO velocity by a 3D ellipse, described mathematically by curvature values (W_{ij}) or by Vfast (small axis), Vslow (long axis) and θ, the azimuth of Vslow (azimuth of long axis):

$$T^2 = T_0^2 + \frac{X^2}{V^2_{nmo}(\theta)}.$$

where T is the time shift calculated by the E.A.P. procedure, X is the offset, and V is the RMS velocity.

$\frac{1}{V^2_{nmo}(\theta)}$. can be expressed in terms of Vfast, Vslow and θ or in terms of curvature coefficients (W_{ij}) of a 3D ellipse and θ (Figure 17).

By using the offset and azimuth-dependent time shifts T of the E.A.P. in the equation $T^2 = T_0^2 + [W_{11} \cos^2\theta + 2 W_{12} \cos\theta \sin\theta + W_{22} \sin^2\theta] X^2$,

we can find the unknown W_{ij} coefficients of the best-fitting 3D ellipse using a least-square method that also estimates the fitting error.

The transformation of these RMS velocity attributes into Interval Velocity attributes is performed by use of a Dix-like equation, that incorporates ellipse coefficients (W_{ij}).

From these calculations, the following four volumes of data are generated:

(1) The fastest interval velocity (Vf),

(2) The azimuth of this fastest interval velocity (azimuth of the ellipse's small axis),

(3) The difference between the fastest and the slowest (azimuthally orthogonal) interval velocity. (After normalization [(Vf-Vs) / Vf], we can call this attribute "the interval velocity anisotropy"), and

(4) The estimated error of the fitting procedure.

The shale reservoir is 60 to 84 ms thick (two-ways traveltime). Since the interval velocity attributes were calculated from the RMS velocity with a sliding 100ms vertical window, to interpret these attributes, I created a phantom horizon (Figure 17) through the middle of the reservoir, by simple addition and division by 2 of the time horizons that define the top and bottom boundaries of the shale reservoir. Such an horizon minimizes contamination from overlying and underlying lithologies. Then, I extracted the values of the four attributes above from the plane of the phantom horizon to create ASCII numerical files, crossplots and maps.

I display histograms of Vfast and Vfast-Vslow in Figures 19 & 20. The fast interval velocity varies between 14,500 ft/s (4350 m/s) and 17,500 ft/s (5250 m/s). Vfast-Vslow ranges from 0 to 2,000 ft/s (600 m/s), with a peak at 600 ft/s (180 m/s). Therefore, the velocity anisotropy goes up to ~14%, while the mean is closer to 5%.

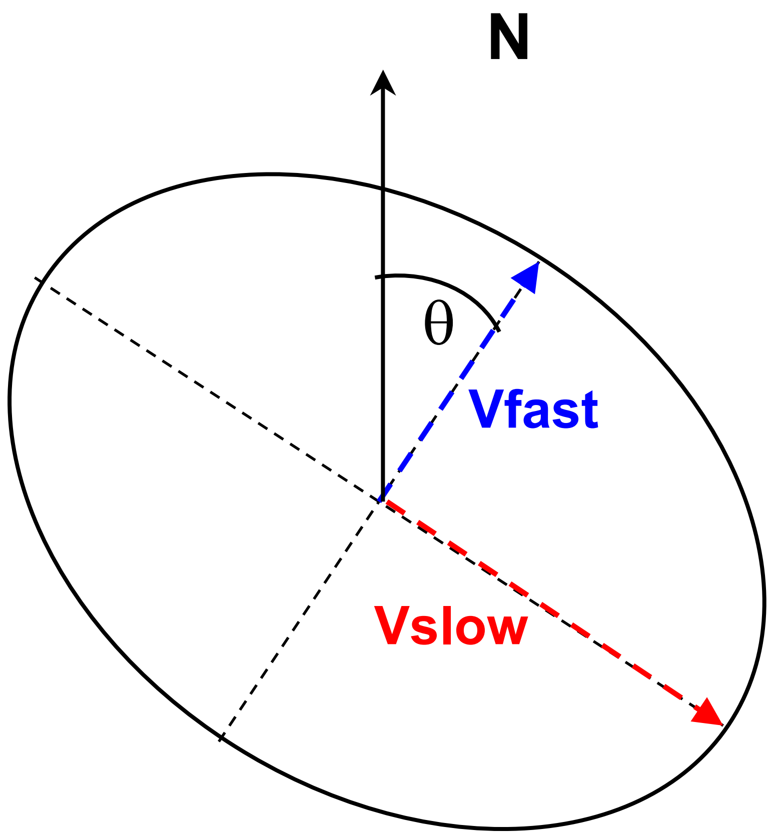

Figure 17: Variation in NMO velocity defined by the best-fit ellipse. This ellipse is characterized by Vfast, Vslow and θ, the angle between Vfast and the North.

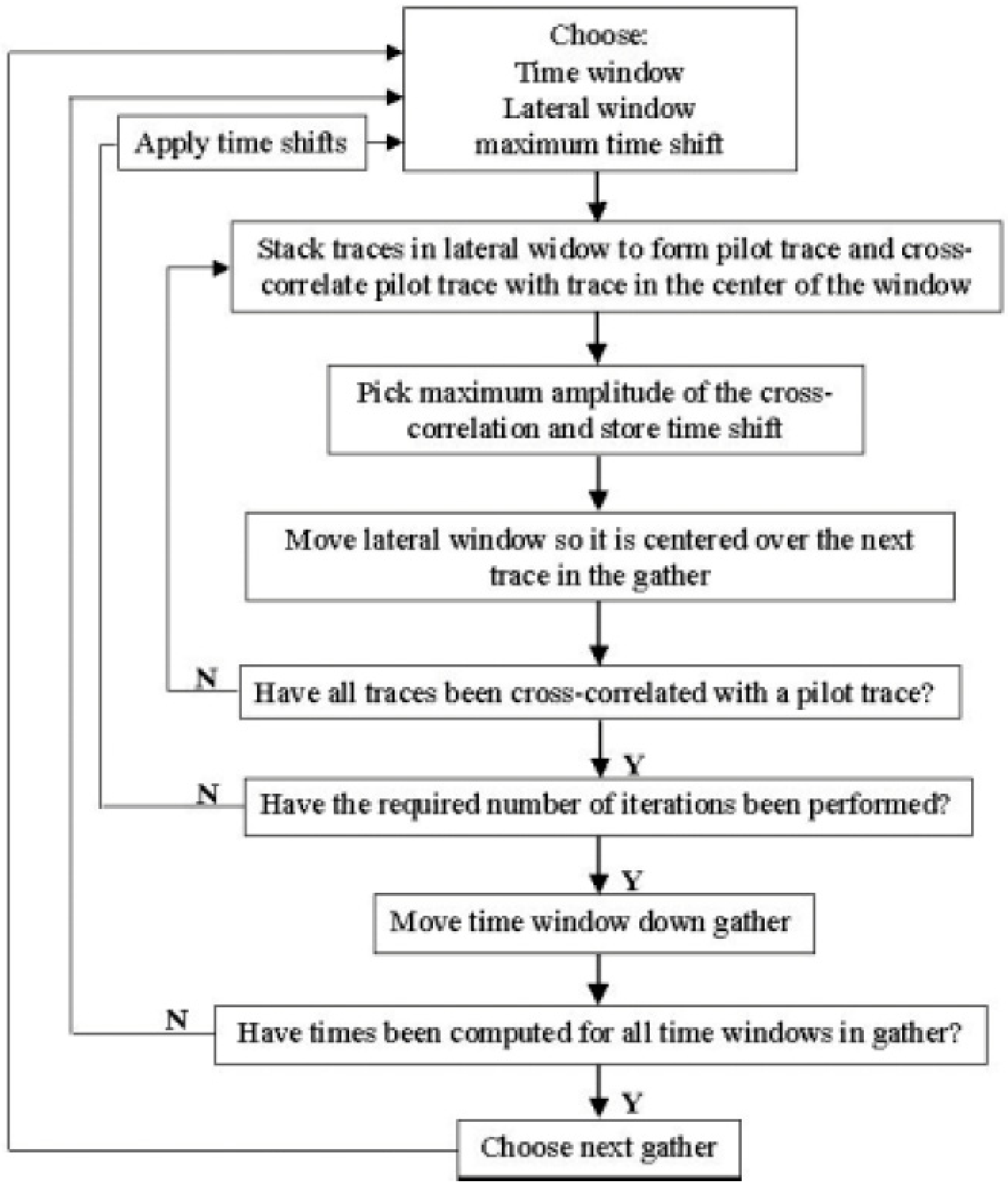

Figure 18: Event Alignment Procedure (E.A.P.), from Edward Jenner, 2001

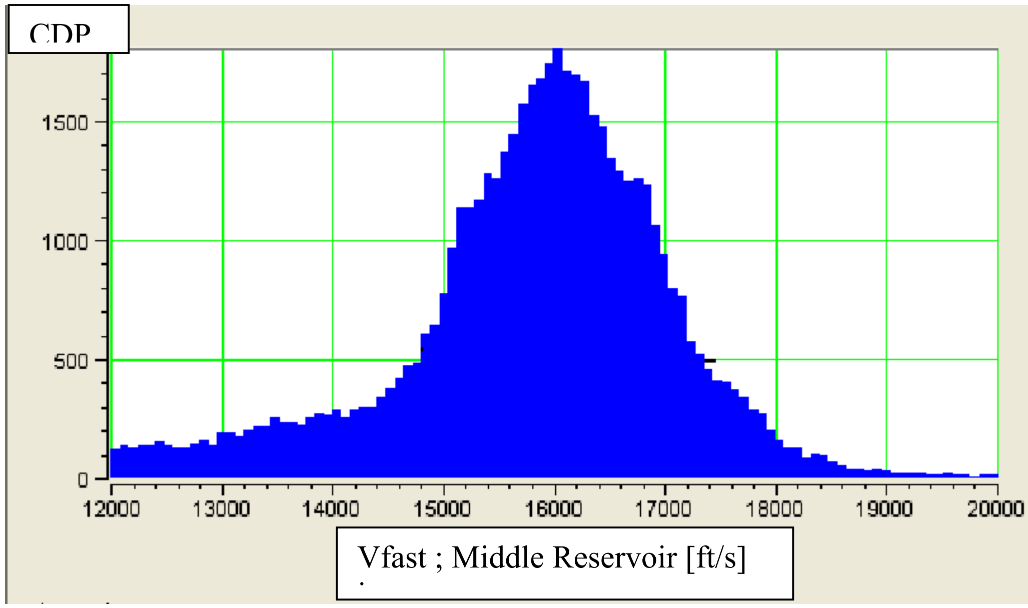

Figure 19: Histogram of Vfast [ft/s] in the middle of the reservoir. Median value ~16,000 ft/s (4800 m/s)

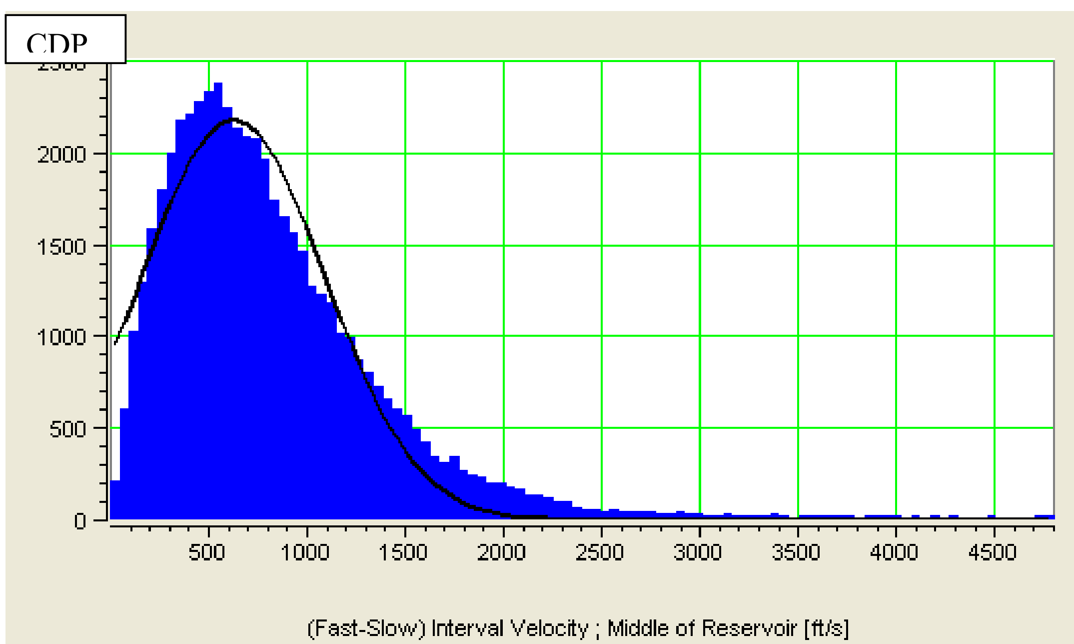

Figure 20: Histogram of (Vfast – Vslow) [ft/s] in the middle of the reservoir. Median value ~800 ft/s (240 m/s)

4.2. Curvature

Al-Dossary and Marfurt (2005) developed algorithms to create volumes of curvature attributes, using time-migrated post-stack data.

I have chosen Kmax, the maximum curvature defined by Roberts (2001), as it shows concave as well as convex shapes, for mapping reflectors. Positive values show convex areas, such as ridges or domes, and negative values concave areas, such as bowls or valleys. For linear numerical correlations, it is better to use the most positive (K+) and most negative (K-) curvature volumes rather than Kmax.

Low values for the minimum curvature (Kmin) correspond to flat areas (horizontal or dipping), as well as areas with one planar direction, like ridges and valleys.

All these curvature attributes are calculated from post-stack, time migrated

data. Curvature is a measure of reflector shape rather than rock properties. As these shapes are not altered by hydrofracs, E.U.R. of all wells (including the ones drilled before the 3D seismic acquisition) can be used to test them.

4.3. Inter-Azimuth Similarity Attribute

This new attribute was presented at the 2004 SEG annual meeting (Al-Dossary *et al*, 2004). The first step consists of division of the data into different volumes (Figure 21), by azimuth and offset. Since we interpret the main present day regional stress azimuth as being SW-NE (from the World Stress Map, image logs and micros-seismic monitoring of hydrofracs), the data were subdivided into four volumes, SW-NE near offsets (“Nears”), SW-NE far offsets (“Fars”), SE-NW near offsets, and SE-NW far offsets, that are aligned parallel and perpendicular to the regional maximum horizontal stress. Near offsets have an incident angle at the target depth between 0° and 20°, while the far offsets have an angle of incidence between 20° and ~45°.

The similarity was calculated, trace by trace, between volumes of data having the same range of incident angles, but a different azimuth, to produce volumes called “inter-azimuth similarity” (Figures 22 & 23). We selected first a 20 ms vertical window, and later produced two new volumes with an 80 ms vertical window.

I used these volumes to extract maps of similarity at different levels (Figure 24). Our algorithm searches for the best match within the vertical window, to take into account time shifts between the two far offset volumes due to velocity estimation errors. Time-delay volumes (Figure 25) were generated; not surprisingly, they show larger time shifts between the two far-offset volumes compared to the two near-offset volumes.

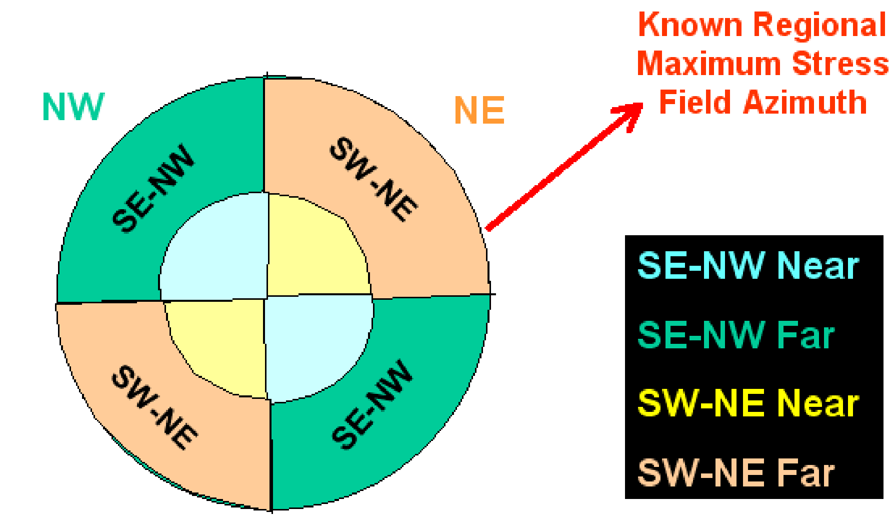

Figure 21: Division of 3D wide-azimuth seismic data into four offset-azimuth limited stacks

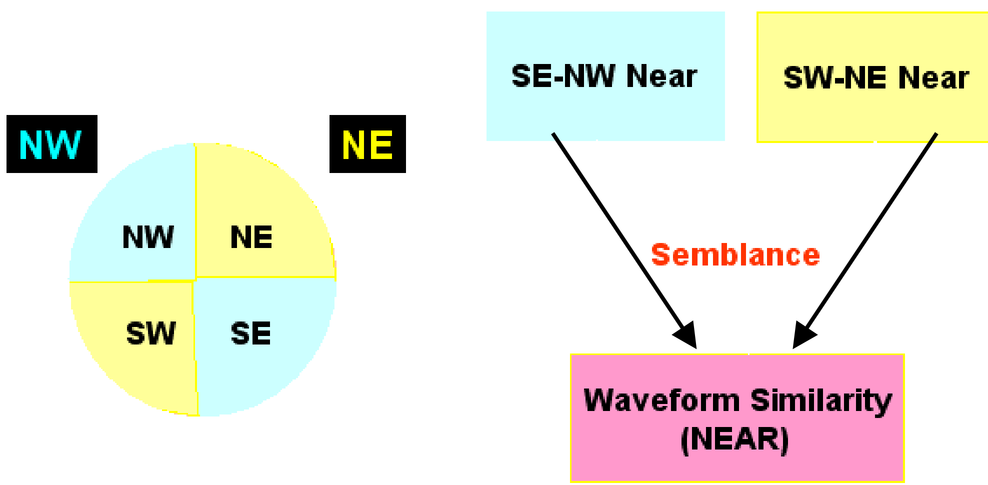

Figure 22: Creation of new data volumes by cross-correlation, trace by trace, of the SW-NE and SE-NW volumes, Near offset.

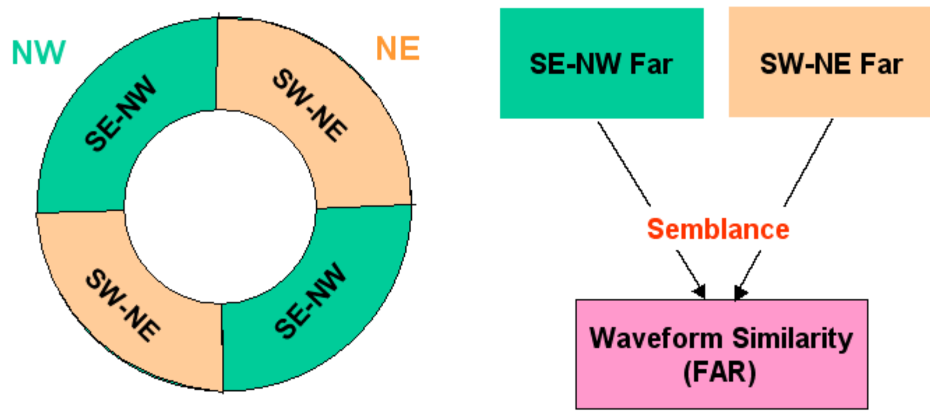

Figure 23: Creation of new data volumes by cross-correlation, trace by trace, of the SW-NE and SE-NW volumes, Far offset.

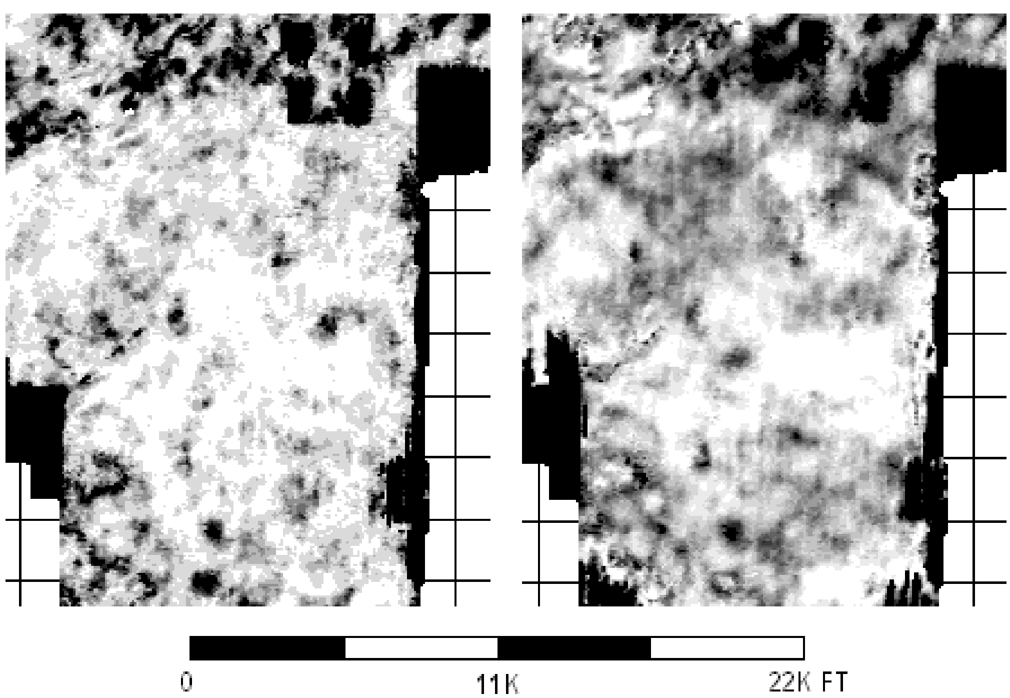

Figure 24: Reflector at the bottom of the reservoir. Near-offset and far-offset inter-azimuth similarity volumes. Traces in black areas are highly dissimilar, traces in white areas are identical (in the SW-NE and the SE-NW volumes).

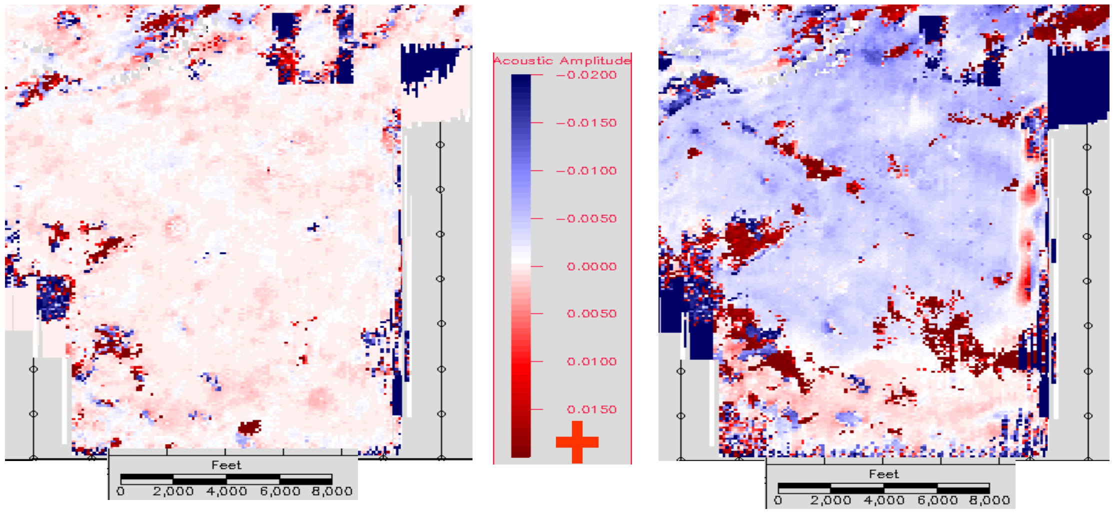

Figure 25: Time shift to correlate optimally near-offset (left) and far offset (right) SW-NE and SE-NW volumes. Low value areas are white, high values are red (NW time > NE time) or blue (NW time < NE time).

5. CORRELATION OF AZIMUTHAL INTERVAL VELOCITY ATTRIBUTES WITH WELL DATA

5.1. Assumptions

If aligned vertical fractures and / or maximum horizontal stress are not present, or exist in one azimuth only, the 3D ellipse fitting is adequate to characterize the velocity field. If two sets of vertical parallel cracks are present, a more complicated 3D shape should be used.

The following assumptions were made to interpret the three velocity attributes volumes calculated by Axis:

- A small value of Vfast indicates a low horizontal stress, and/or presence of multi-azimuth fractures. Hydrofracs should create a large network of multi-azimuth fractures when Vfast is small, and therefore, a low Vfast is good for production.
- A large Vfast indicates areas of high horizontal stress and/or the absence of natural multi-azimuth fractures. This is bad for production.
- A small Vfast–Vslow (azimuthal velocity anisotropy), shows areas without vertical aligned fractures and without azimuthally-oriented dominant horizontal stress. Multi-azimuth fractures can be present. This is good for production, as the creation of a network of interconnected fractures should be easier when Vf-Vs is small.
- A large value of Vfast–Vslow indicates the presence of vertical aligned fractures and/or anisotropic horizontal stress. Their azimuth corresponds

to the azimuth of Vfast. Hydrofracs, done in areas showing a strong interval velocity variation with azimuth, induce non-connected, parallel, aligned fractures, and these are detrimental to production.

In many parts of the world, present day stress and natural fractures are correlated. However, in this reservoir, they are not correlated because the horizontal stress azimuth has changed since the creation of the fractures. Natural fractures in this field are rare, thin (being oriented SE-NW, orthogonal to the present horizontal stress), and are often calcite-filled. Therefore, I suppose that they have a small effect on seismic velocities.

5.2. Correlation of azimuthal interval velocity with E.U.R.

I correlated Estimated Ultimate Recovery (E.U.R.) with seismic attributes, dividing my well control into two populations, ~60 wells drilled and hydrofrac'd before the 3D seismic acquisition, and ~62 wells drilled after the 3D seismic acquisition. I divided the wells into two groups because hydrofracs done before the 3D seismic acquisition are likely to have changed the stress and fractures present in the earth, especially near the wells. Deleting wells near the survey edges, where azimuthal seismic attributes are unreliable, improved the correlations. The limits of the area containing meaningful values vary with the attribute considered, thus, the number of wells used for the crossplots also varies. The following attributes were crossplotted against E.U.R.:

- Fast interval velocity extracted at mid-reservoir level. The normalized cross-correlation coefficient, ρ is equal to -0.38 (wells drilled after 3D seismic survey), which is a significant inverse correlation, taking the number of wells into account, and is our best numerical correlation to date (Figure 26). ρ is only –0.15 using the wells drilled before the 3D seismic acquisition.

- (Fast - Slow) interval velocity extracted at mid-reservoir level. There is a small but still significant inverse correlation: ρ = -0.20 (Figure 27).

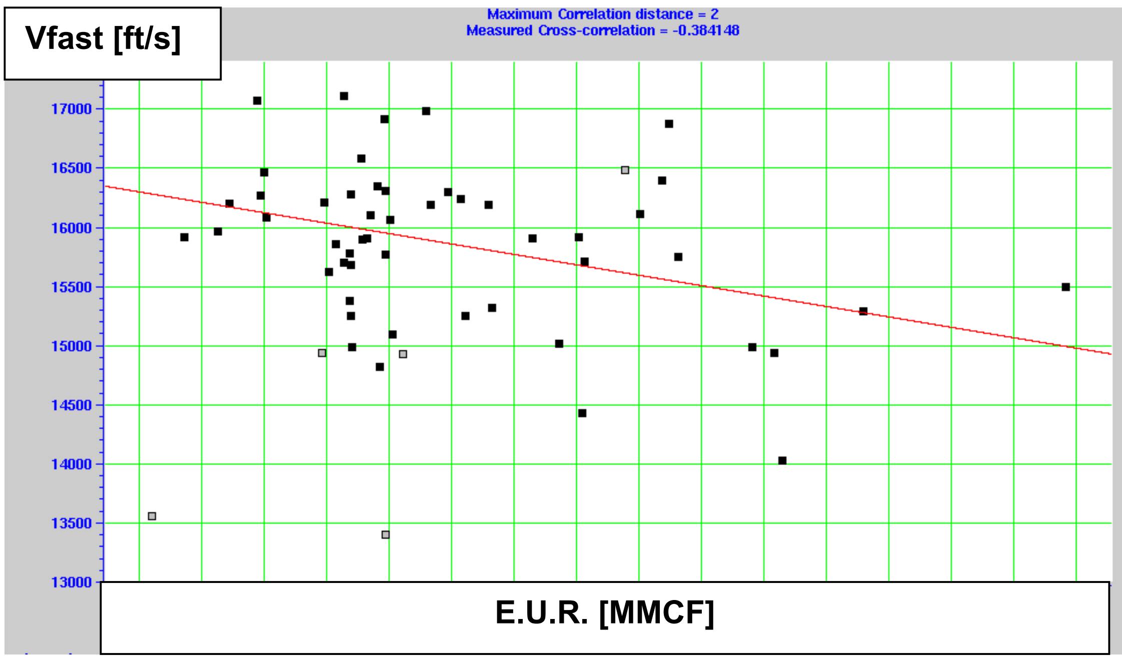

Figure 26: E.U.R. of wells drilled after 3D seismic survey versus Vfast in the reservoir; ρ = -0.38. Gray dots: wells removed (unreliable seismic data, too close to edge of survey)

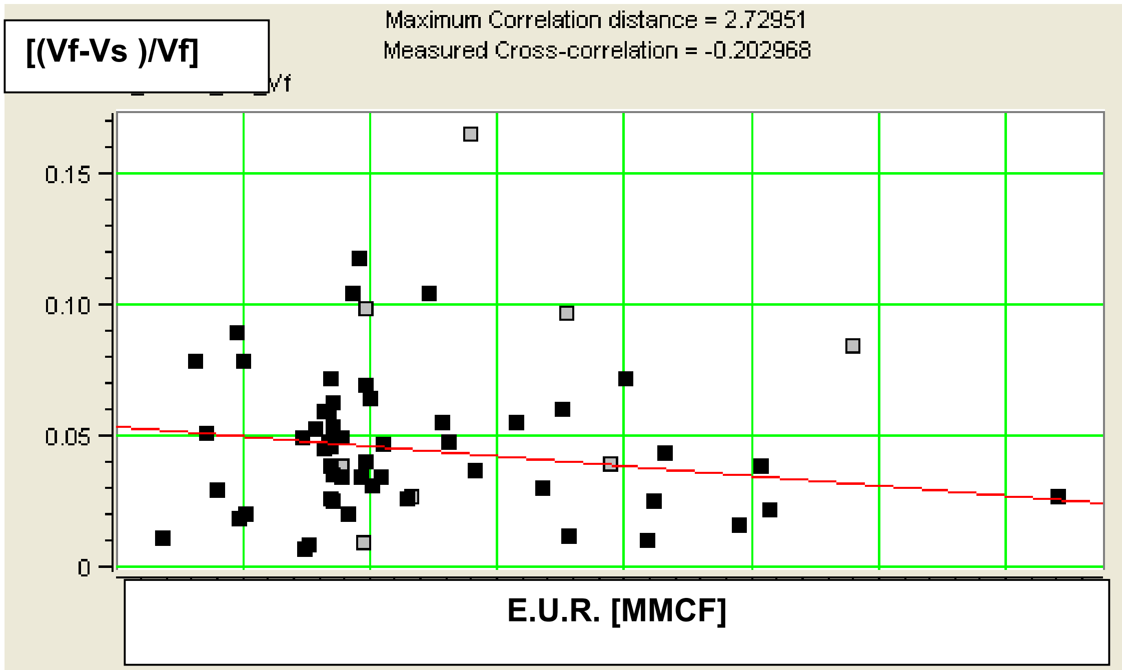

Figure 27: E.U.R. of wells drilled after 3D seismic survey versus [(Vfast-Vslow) / Vfast] in the reservoir; ρ = -0.20

5.3. Multi-layer maps: azimuthal interval velocity, E.U.R. and Microseismic

Crossplots do not display spatial correlations between attributes, as shown by Nissen *et al* (2004). For this reason, I made maps with the available seismic attributes and well data. One of the major challenges with interpretation of multi-attributes is to co-render them on a single display. I used icons (e.g. arrows, bars, triangles, diamonds) to co-render three attributes, a method developed at Lynn Incorporated (Lynn and Simon, 2002): the icon azimuth is the azimuth of Vfast (AzimVf), its length is proportional to Vfast, and its color displays the difference between the fast and the slow interval velocity (Vf-Vs). This type of display has advantages and disadvantages compared to more traditional, color-filled contour maps. One icon (like arrows) can display the information of three attributes; the icons can be easily overlaid on traditional gray-filled contour maps, and they give the interpreter an immediate knowledge of the azimuth of Vfast. But the disadvantage is the necessity to plot these icons on very large displays, to decimate them, or to zoom in to be able to distinguish them clearly.

I overlaid the E.U.R. of the wells drilled before the 3D seismic acquisition on top of the azimuthal interval velocity attributes within the reservoir (Figure 28), then the E.U.R. of the wells drilled after the 3D seismic acquisition (Figure 29).

As the length of the icons is the least perceptible feature of our icons, and corresponds to our best ρ attribute, Vfast, I made a new icon map with Vfast being represented by the color instead of the length, and Vf-Vs the length instead of the color (Figure 30).

Our best benchmark for seismic attributes is the fracture pattern defined by microseismic experiments. I overlaid the azimuthal interval velocity icons on top of microseismic-defined induced fractures, and found an excellent correlation using two wells drilled and hydrofrac'd after the 3D seismic acquisition. By contrast, the correlation between azimuthal interval velocity and induced fractures around wells drilled before the 3D seismic acquisition is very poor.

Figure 31 shows that the dominant induced fractures around this well (drilled after 3D seismic acquisition) are oriented SW-NE, as around the other monitored wells. But this specific well also has many orthogonal (SE-NW) induced fractures, which link the SW-NE fractures. This explains the excellent gas production of this well.

By contrast, the well on Figure 32 is a poor producer, the SW-NE induced fractures being very long but not linked to each other by orthogonal pathways.

I will discuss in detail the relation between induced fractures and interval velocity attributes in a subsequent section (5.4).

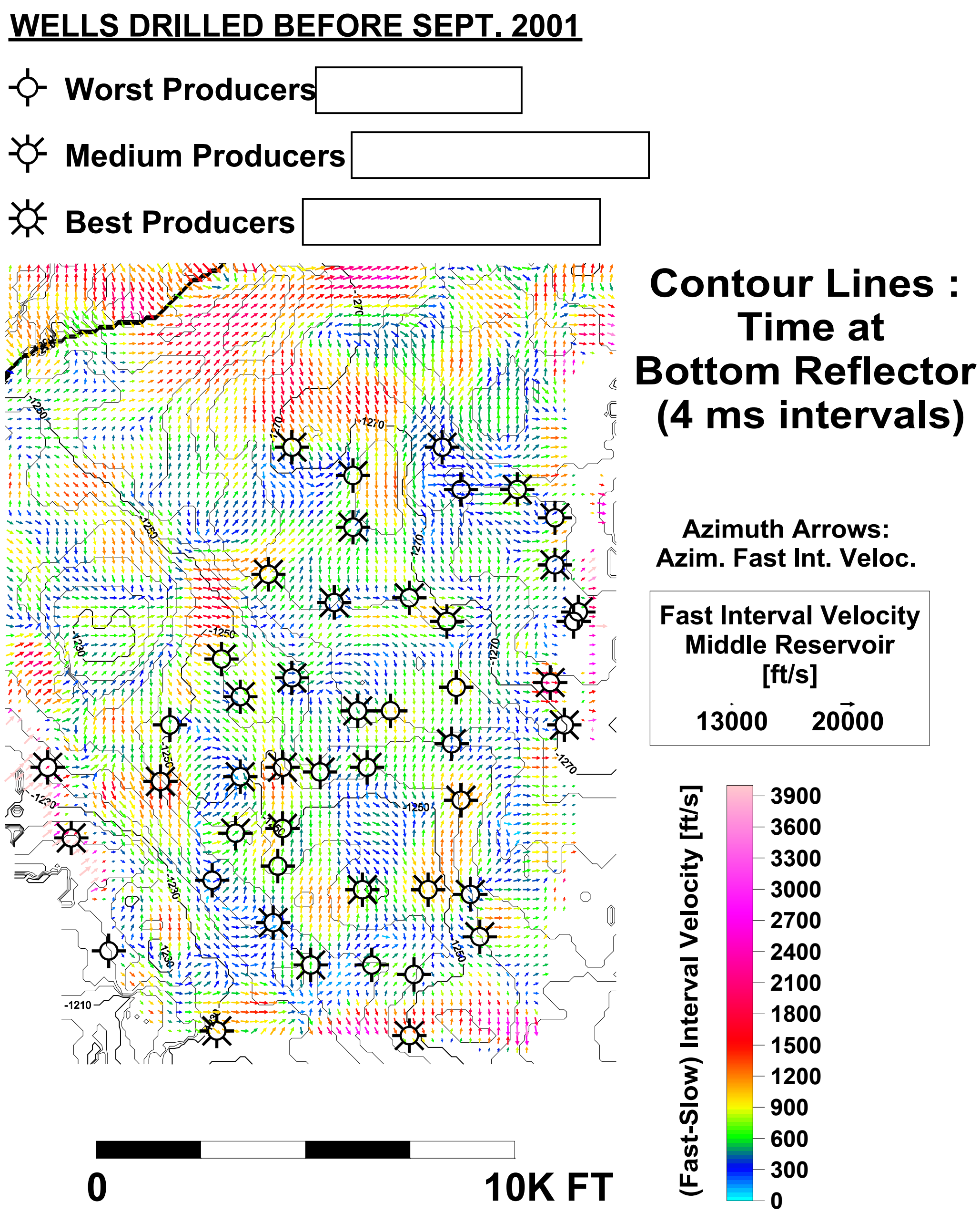

Figure 28: Interval velocity attributes and wells drilled before 3D wide-azimuth seismic acquisition

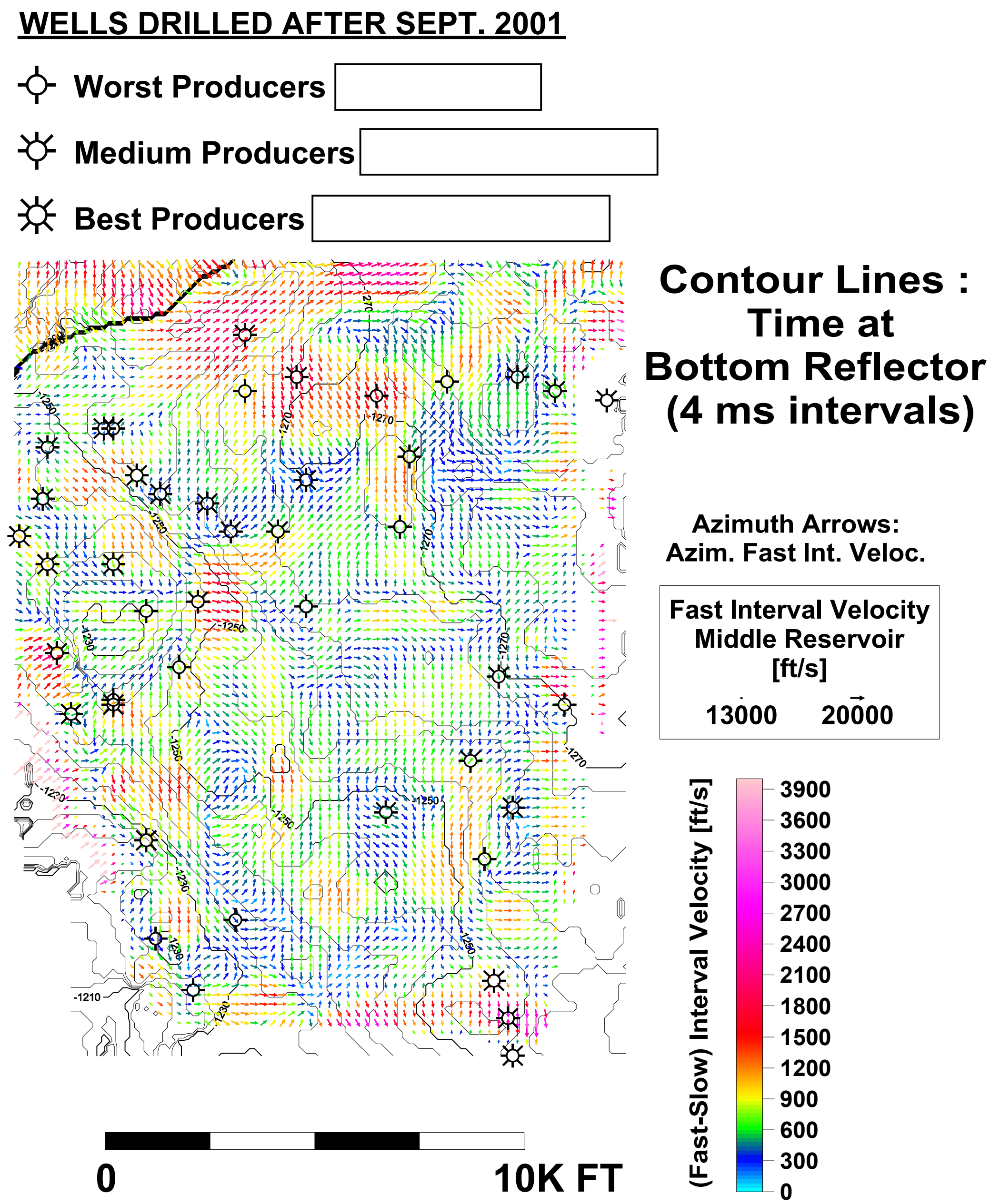

Figure 29: Interval velocity attributes displayed by arrows; wells drilled after 3D wide-azimuth seismic acquisition

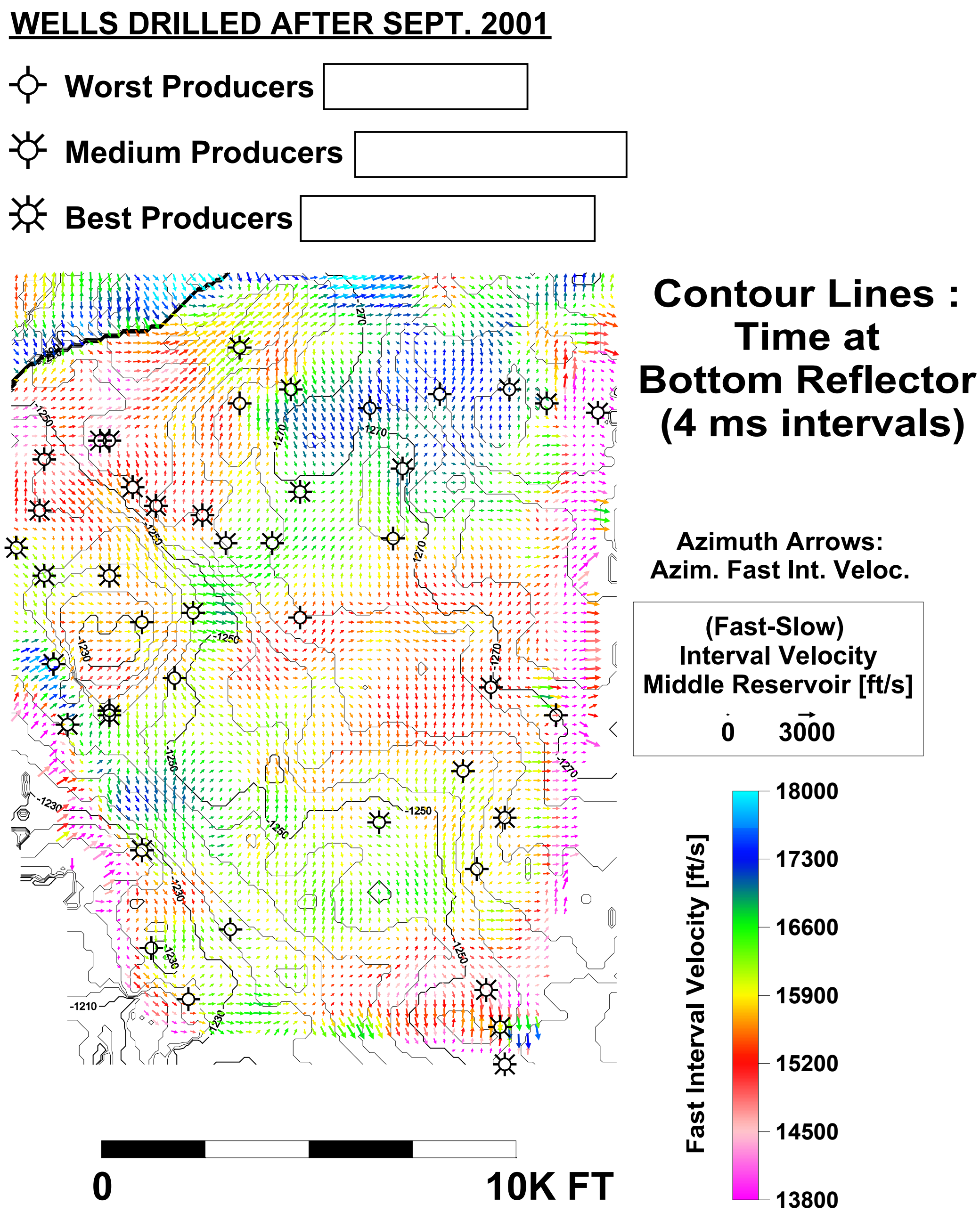

Figure 30: Interval velocity attributes displayed by arrows and wells drilled before 3D wide-azimuth seismic acquisition. But here the color of the arrows represents Vfast instead of Vfast-Vslow, and their length Vfast-Vslow instead of Vfast. Good wells are often in warm color (small Vfast) areas, bad producers in cold color areas (large Vfast).

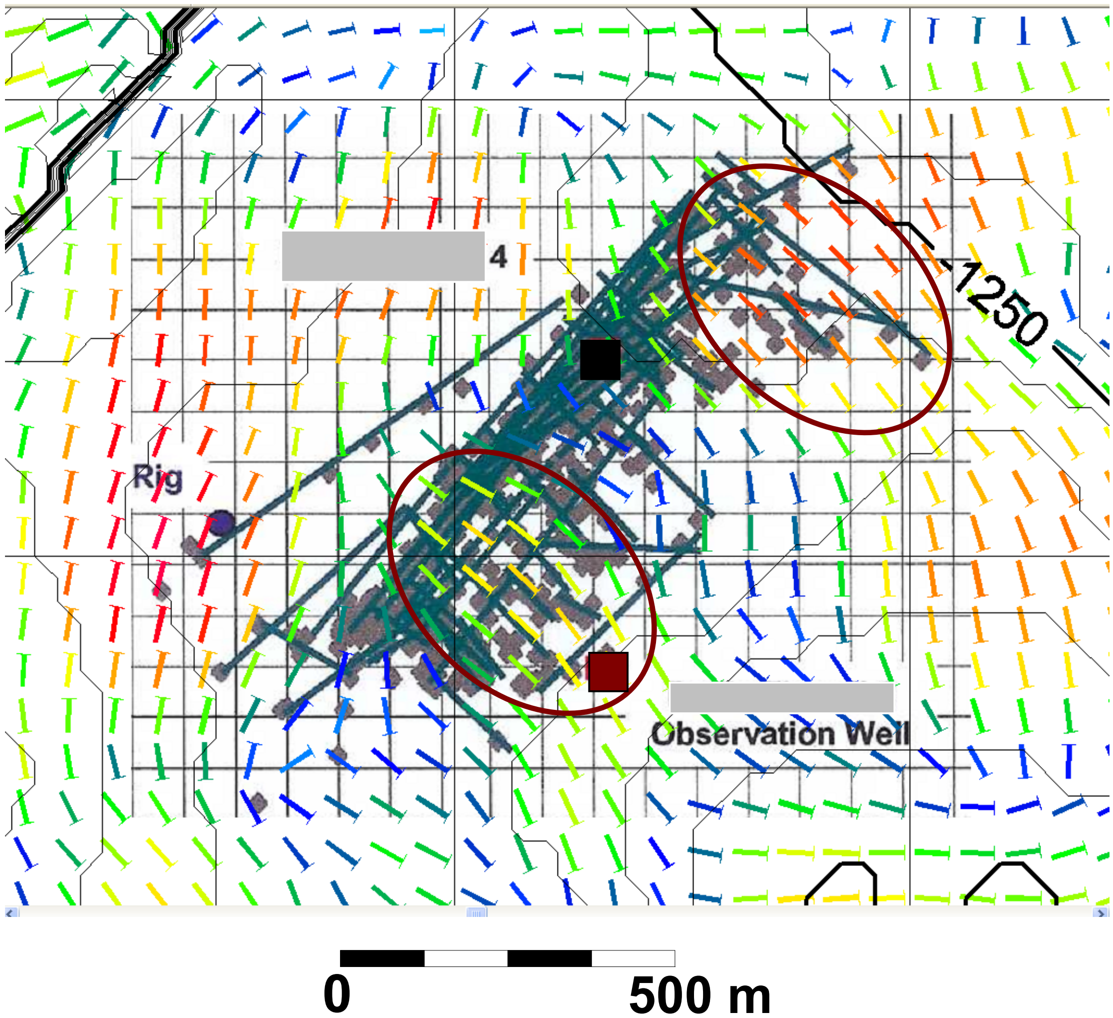

Figure 31: Induced fractures by hydrofracs defined by microseismic measurements: grey dots are micro-earthquake events, dark green lines are interpreted fractures. Black square: injection well MT4. Brown square: observation well. High production well. Bars represent interval velocity attributes. Warm colors mean small anisotropy, cold colors high anisotropy (same scale as Figure 29). Length of bars is proportional to Vfast. Azimuth of bars corresponds to azimuth of Vfast.

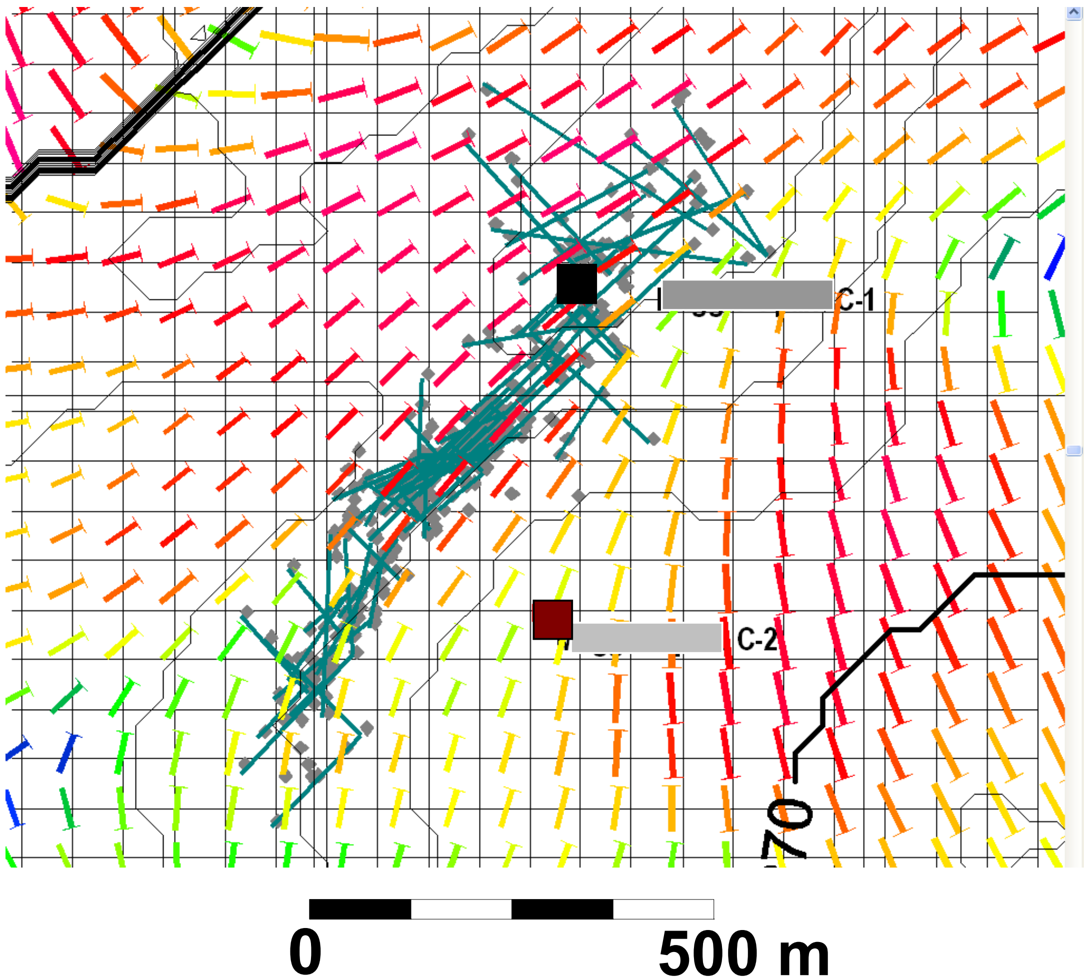

Figure 32: Induced fractures by hydrofracs defined by microseismic measurements: grey dots are micro-earthquake events, dark green lines are interpreted fractures. Black square: injection well MS1. Brown square: observation well. Bars represent interval velocity attributes. The scales are the same as in Figure 29. Low production well.

5.4. Discussion of the azimuthal interval velocity results

The absolute values of ρ were generally higher using the wells drilled after the 3D seismic acquisition, compared to the wells drilled before. Moreover, the correlation between azimuth of Vfast and induced fractures around wells drilled after the 3D seismic acquisition does not exist for the four wells drilled before the 3D seismic acquisition. These findings suggest that the horizontal stress regime in the reservoir has been changed by the hydrofracs.

Taking into account that I used a far from perfect benchmark, E.U.R., but a large number of wells (up to 60 drilled after the 3D seismic acquisition), the normalized cross-correlation of –0.38 for Vfast can be considered to be very good, and is consistent with our hypothesis of an inverse relation between strongly oriented horizontal stress and creation of a wide, multi-azimuth, well-connected network of fractures by hydrofracs. The map in Figure 30 confirms an inverse correlation between E.U.R. and Vfast.

However, we expected a larger inverse correlation (see assumptions, 5.1.) than ρ = -0.20 between Vf-Vs and E.U.R.. Since the normalization of Vf-Vs gives a better assessment of interval velocity anisotropy, I divided Vf-Vs by Vf, and re-made a crossplot with E.U.R. of wells drilled after the 3D seismic acquisition. Unfortunately, the ρ did not improve (still 0.20).

Figure 31 is very interesting but challenging. If there are more SE-NW oriented induced fractures than around the five other hydrofrac'd wells studied by microseismic measurement, the induced fracs are still predominantly oriented SW-NE. The azimuth of Vfast is SE-NW. It seems that the interval velocity is more sensitive to local SE-NW "features" than to the regional horizontal stress field. It is possible that these SE-NW features are open natural fractures. The F.M.I. log for this well shows the presence of a small number of partially open, partially cemented natural fractures. Since resistivity logs are able to image only up to a very short distance from the well, it is possible that the natural open fracture's density in this area is higher than suggested by the F.M.I. log analysis. It is evident, too, that there are more SE-NW micro-seismic events recorded in areas of medium velocity anisotropy (Vf-Vs = ~800 ft/s; brown ellipses in Figure 31) compared to areas of low anisotropy (cold color bars).

Figure 32 shows that the long, narrow SW-NE area with induced fractures corresponds to high Vfast, high Vf-Vs (~1400 ft/s), and SW-NE azimuth of Vfast.

The SW-NE dominant horizontal stress field shown by induced fractures corresponds to the dominant regional stress field, and is probably reinforced by the proximity of the main normal right lateral, strike-slip fault (see 2.3).

Figure 31 shows that SE-NW induced fractures, essential for good production, are associated with a SE-NW (135°) Vfast azimuth and Vf-Vs above 500 ft/s (152 m/s). Therefore, I took the azimuth of Vfast extracted at mid-reservoir level and deleted the values when the associated (Vf-Vs) was smaller than 500 ft/s.

Next, I looked at the E.U.R. of the wells drilled after the 3D seismic acquisition, and divided them into four groups, according to the azimuth of Vfast. The azimuth of group one is centered on 0°, the second group on 45°, the third group on 90° and the last group on 135°. See Figure 33 for more details. The average EUR of wells with SW-NE Vfast azimuth is only 843 MMCF, but the average EUR of wells with SE-NW azimuth is 1390 MMCF, which is consistent with Figure 31, and it is a very positive and important result.

Azim Vfast	**Azimuth**	**# Wells (Vf-Vs) > 500 ft/s Drilled after 3DS**	**Avg EUR**
0° to 22.5° and 157.5° to 180°	S-N	15	17
22.5° to 67.5°	SW-NE	7	**12**
67.5° to 112.5°	E-W	9	15
112.5° to 157.5°	SE-NW	10	**20**

Figure 33: Average E.U.R. of wells divided into four groups with different Vfast azimuth. The wells considered have a (Vf-Vs) larger than 500 ft/s.

6. CORRELATION OF CURVATURE WITH WELL DATA

6.1. Assumptions

One must be very cautious interpreting curvature attributes. Their relation to stress and vertical fractures is not obvious. For example, we might think at first that a linear convex area (a “ridge”) is an indicator of aligned vertical fractures above and parallel to the ridge due to orthogonal extensional relief of stress. But if the top of the ridge is far enough above the level studied, we could be in an area of compressional stress perpendicular to the ridge, and fractures would be orthogonal to the ridge. The plane where the change between these two stress regimes occurs is called the neutral plane (Roberts, 2001).

When fractures are mainly created parallel to the highest stress direction, a network of secondary, orthogonal fractures is also created due to the weak cohesion resulting from the stress release (Stearns and Friedman, 1972).

I assume that:

- Areas of large K+ and / or K- are more susceptible to be areas of stress relief and fracturing.
- Linear areas of large Kmax, visible on maps, are more susceptible to indicate anisotropic horizontal stress and / or fractures (but we do not know if this horizontal stress is parallel or orthogonal to the lineaments).

6.2. Correlation of curvature with E.U.R.

I crossplotted the following attributes with E.U.R. of wells drilled – and hydrofrac'd – before the 3D seismic survey, and later with wells drilled after the 3D seismic survey. I obtained the following results with the latter:

- Most positive curvature (K+) at the bottom reflector: ρ = -0.09
- K+ at the top reflector: ρ = -0.10
- Most negative curvature (K-) at the bottom reflector: ρ = -0.20
- K- at the top reflector: ρ = -0.10

6.3. Multi-layer maps: maximum curvature, E.U.R. and microseismic

I overlaid the E.U.R. of the wells drilled before and after the 3D seismic acquisition on top of:

- Maximum curvature (Kmax) at the top of the reservoir (Figure 40).
- Kmax at the bottom of the reservoir (Figure 35).

The maximum curvature is represented by color contours going from black (+1, convex areas) to white (0, flat areas) to dark brown (-1, concave areas).

I do not see a clear trend in the bottom reflector curvature map, but in the top reflector curvature map, it seems that most good wells, drilled before or after the 3D seismic survey, are located in concave areas, or in plane areas between concave and convex lineaments.

Next, I overlaid the induced-fractures mapped by micro-seismic monitoring (well #5) on Kmax of the bottom reflector (Figure 36a) and Kmax of the top reflector (Figure 36b). The injection well (#7) is an average producer, and was drilled before the 3D seismic acquisition, but this should not affect curvature. The three lines in mauve represent many parallel vertical fractures. There is no evident correlation.

Unlike the previous map, Kmax of the top reflector seems to be correlated to the induced fractures around one of the best producing well (Figure 37).

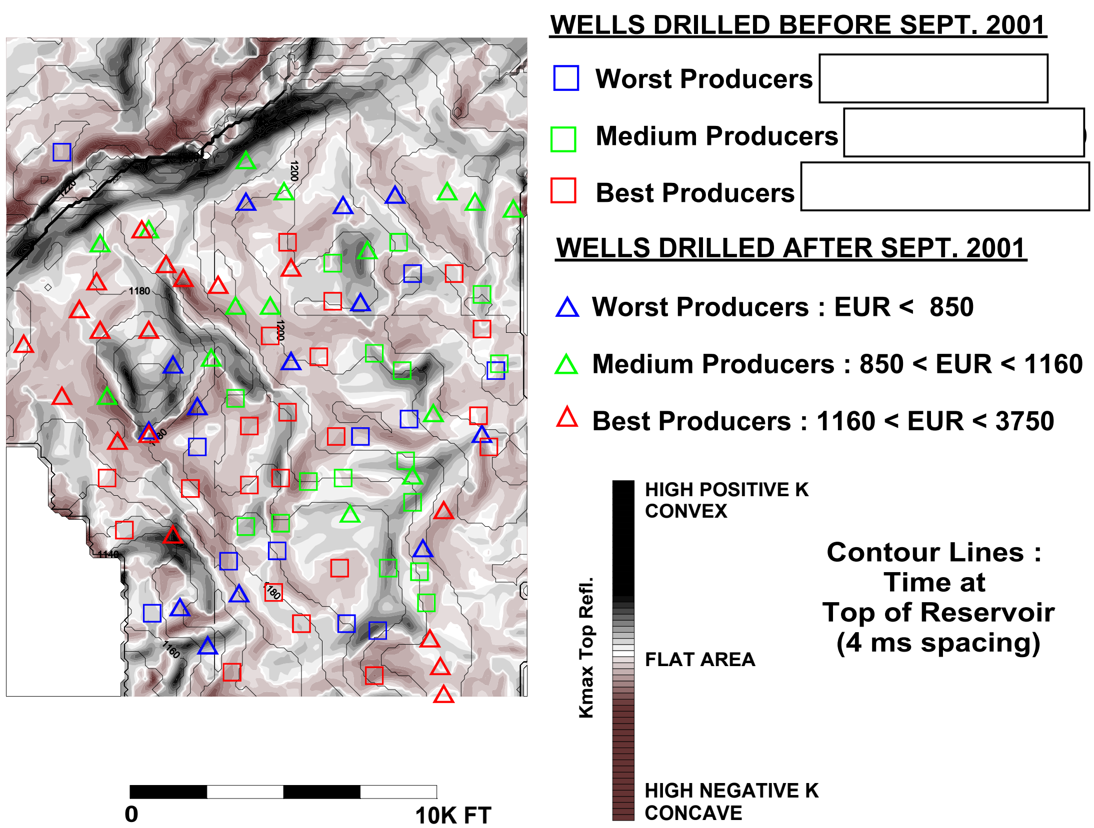

Figure 34: E.U.R. and Kmax of top reflector. The best wells, drilled before or after the 3D seismic survey, are mostly located in concave or plane areas, rarely in convex areas.

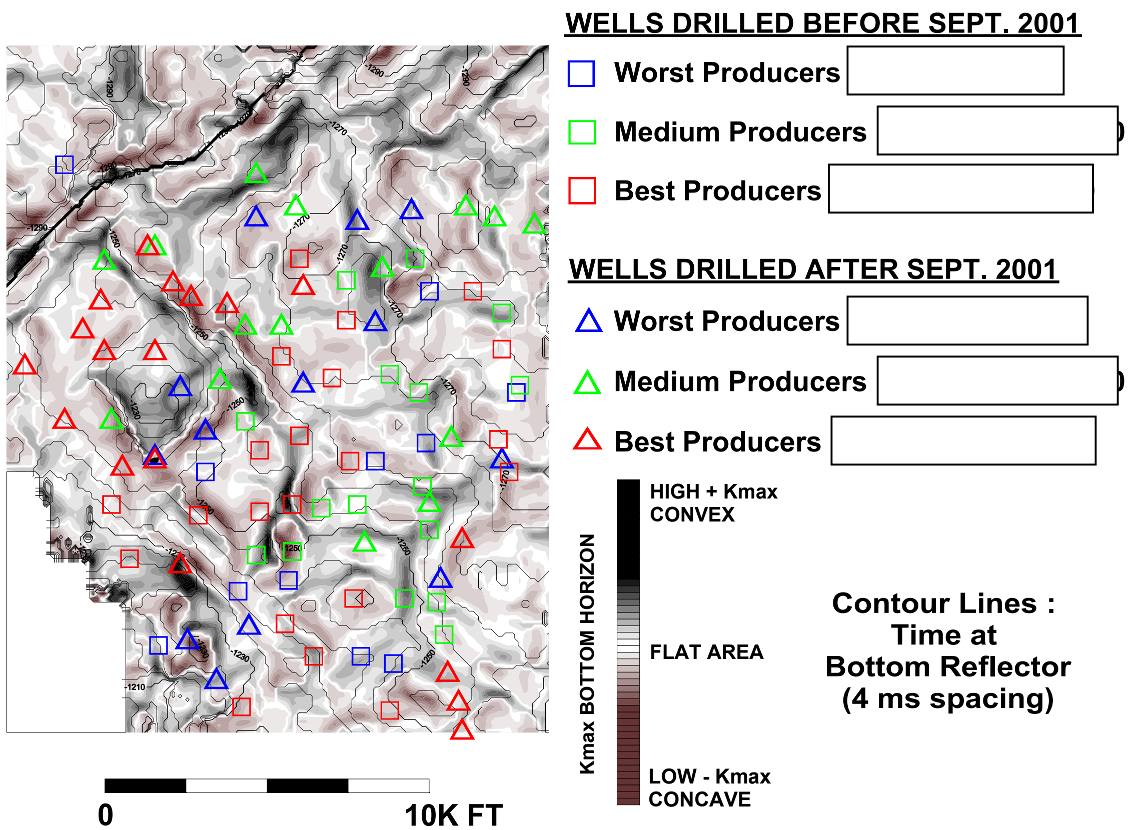

Figure 35: E.U.R. and Kmax of bottom reflector. No evident correlation.

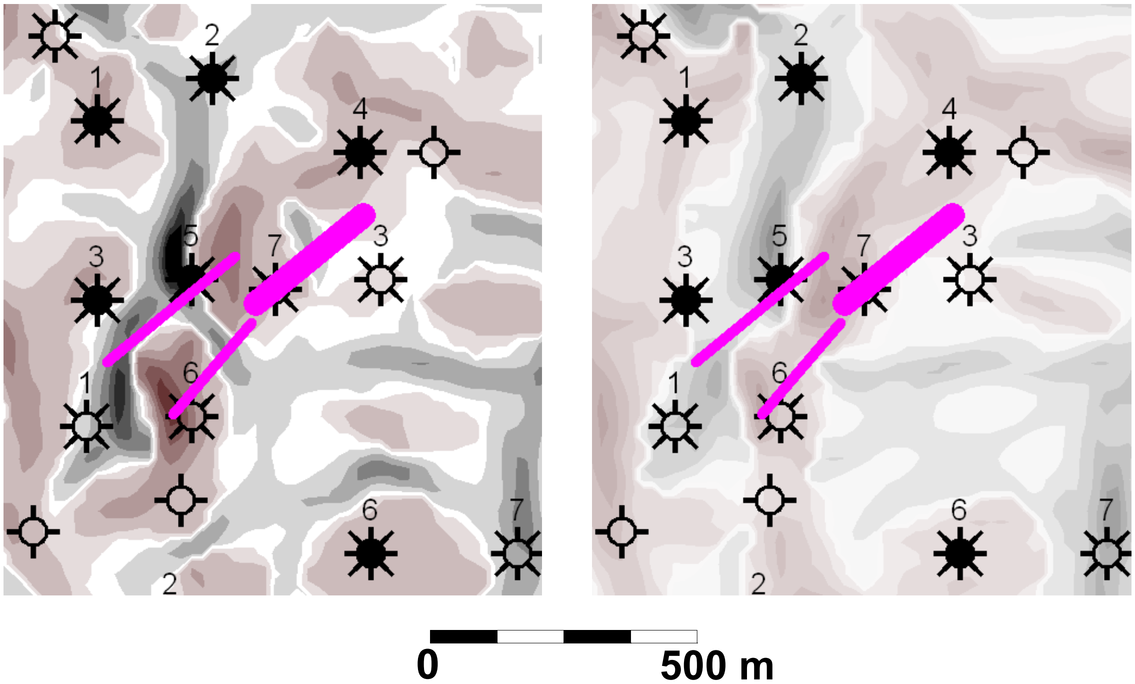

Figure 36a and 36b: Kmax of bottom reflector and Kmax of top reflector, (Brown are concave areas, gray are convex area) overlaid by vertical aligned fractures created by hydrofracs and mapped by micro-seismic experiment (mauve, thick lines; they represent many parallel fractures). Well 7 is the injection well, well 5 is the monitoring well.

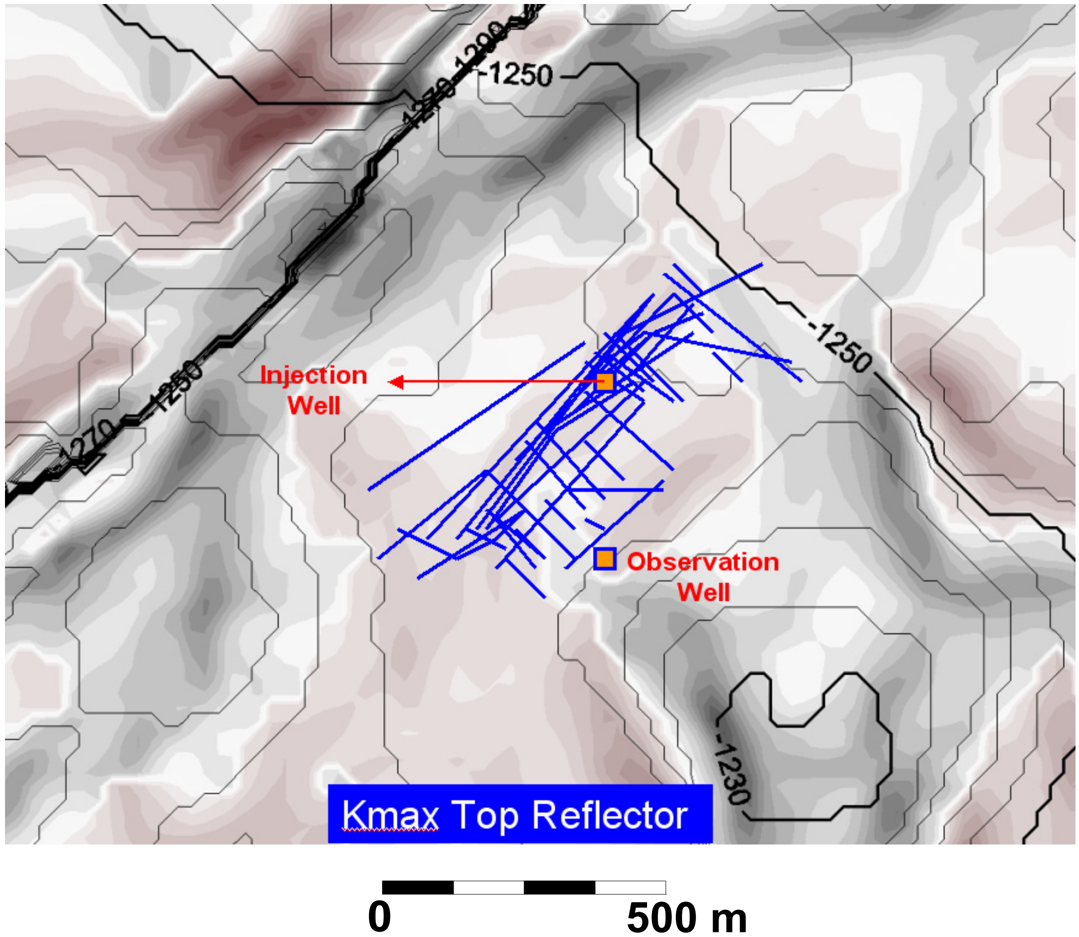

Figure 37: Kmax of top reflector: brown are negative, concave areas, gray are positive, convex areas. The blue lines are vertical fractures created by hydrofracs and mapped by micro-seismic experiment. Induced fractures follow negative curvature area (concave), and they seem to be limited in their NE extension by a convex lineament (ridge).

6.4. Discussion of the curvature results

The very poor normalized cross-correlations found using K+ and K- are probably due to a combination of causes: the ones exposed in 6.1, and the inability of K+ and K-, taken separately, to differentiate linear structures, like ridges and valleys, from isotropic structures, like domes and bowls.

But on a map, an interpreter can distinguish easily between linear and non-linear curved bodies, and Figure 34 seems to show that good wells are most often located in concave or plane areas.

To try to improve our linear numerical correlation, we used combinations of K+ and K-, based on the following table of maximum values for different curvature attributes:

Structure	**K-**	**Kmax**	**K+**	**(K- - K+)**	**|(K- + K+)|**
Bowl	-1	-1	-1	0	+2
Valley	-1	-1	0	-1	+1
Flat	0	0	0	0	0
Ridge	0	+1	+1	-1	+1
Dome	+1	+1	+1	0	+2

-1 and +1 are maxima; they describe very small radius curved bodies. Our data have far smaller absolute values.

To separate linear from non-linear structures, we cross-correlated (K- - K+) with E.U.R., at the bottom of the reservoir. The ρ obtained is still non-significant, 0.12.

These poor correlations could be due to the fact that, if our assumptions are correct, I really should highlight the bowls and domes (isotropic features) instead of ridges and valleys (anisotropic). To do this, I added K+ to K-, took their absolute value, then cross-correlated them with E.U.R.. I obtained a ρ = -0.07 at the bottom reflector.

If the crossplots with E.U.R. could not detect a good cross-correlation with curvature attributes, maps are more interesting. It seems that there is a - weak - correlation between concave or plane, linear areas on the top reflector, and E.U.R. of all wells (Figure 34). Moreover, for one, excellent producer well, there is a correlation between fractures and a concave area, and it seems that a SE-NW ridge is acting as a barrier, limiting the extension of the induced fractures towards the NE (Figure 37).

These maps are incentives to use more sophisticated methods to interpret curvature attributes (see Appendix A).

7. CORRELATION OF INTER-AZIMUTH SIMILARITY WITH WELL DATA

7.1. Assumptions

This attribute should allow detection of amplitude, phase and frequency changes, trace by trace, with azimuth. As we divided the data into two azimuths only (SW-NE and SE-NW), vertical fractures and dominant horizontal stress oriented South-North or East-West cannot be detected.

For the difference of offset between the Nears (less than 20° at reservoir level) and the Fars (more than 20° at reservoir level), it is commonly believed that the Fars are more sensitive to azimuthal anisotropy, because the angle of incidence of the waves with vertical fractures is larger, and more fractures – or horizontal dominant stress – is “seen” by the orthogonal waves.

7.2. Correlation of inter-azimuth similarity with E.U.R.

I crossplotted the following attributes with E.U.R. of wells drilled and hydrofract’d after the 3D seismic acquisition:

- Similarity between SW-NE and SE-NW volumes, near offsets:
    - 20 ms time window, bottom horizon: $\rho = 0.21$
    - 80 ms time window, mid-reservoir: $\rho = 0.14$
    - 20 ms time window, top horizon +6 ms: $\rho = 0.04$
- Similarity between SW-NE and SE-NW volumes, far offsets:
    - 20 ms time window, bottom horizon: $\rho = 0.16$
    - 80 ms time window, Mid-reservoir: $\rho = -0.05$
    - 20 ms time window, top horizon +6 ms: $\rho = 0.06$

7.3. Multi-layer maps: inter-azimuth similarity, E.U.R. and microseismic

The inter-azimuth similarity attribute is represented by gray filled contours.

White to light gray areas are very similar in the SW-NE and SE-NW volumes, dark gray to black areas are highly dissimilar.

I overlaid the E.U.R. of the wells drilled before the 3D seismic acquisition, then of the wells drilled after the 3D seismic acquisition, on top of:

- Similarity SW-NE / SE-NW Nears, bottom horizon, ±10 ms (Figure 38)
- Similarity SW-NE / SE-NW Fars, bottom horizon, ±10 ms (Figure 39)

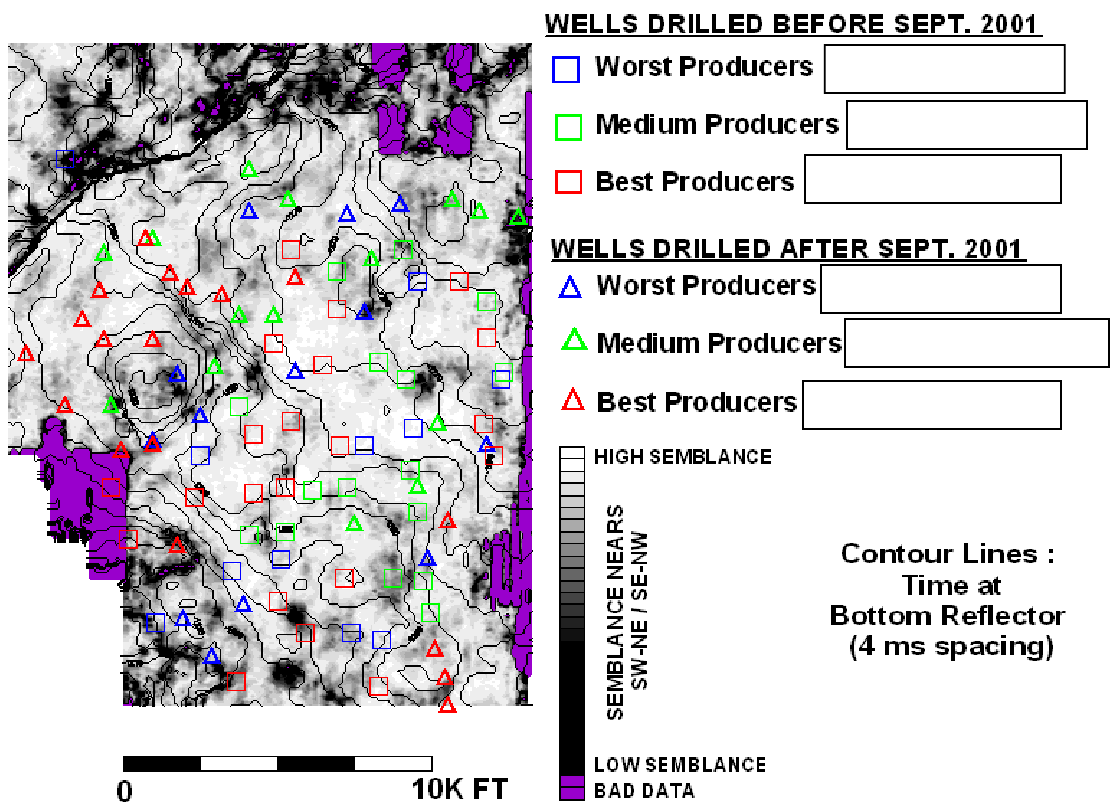

Figure 38: E.U.R. of all wells and inter-azimuth similarity, near offset.

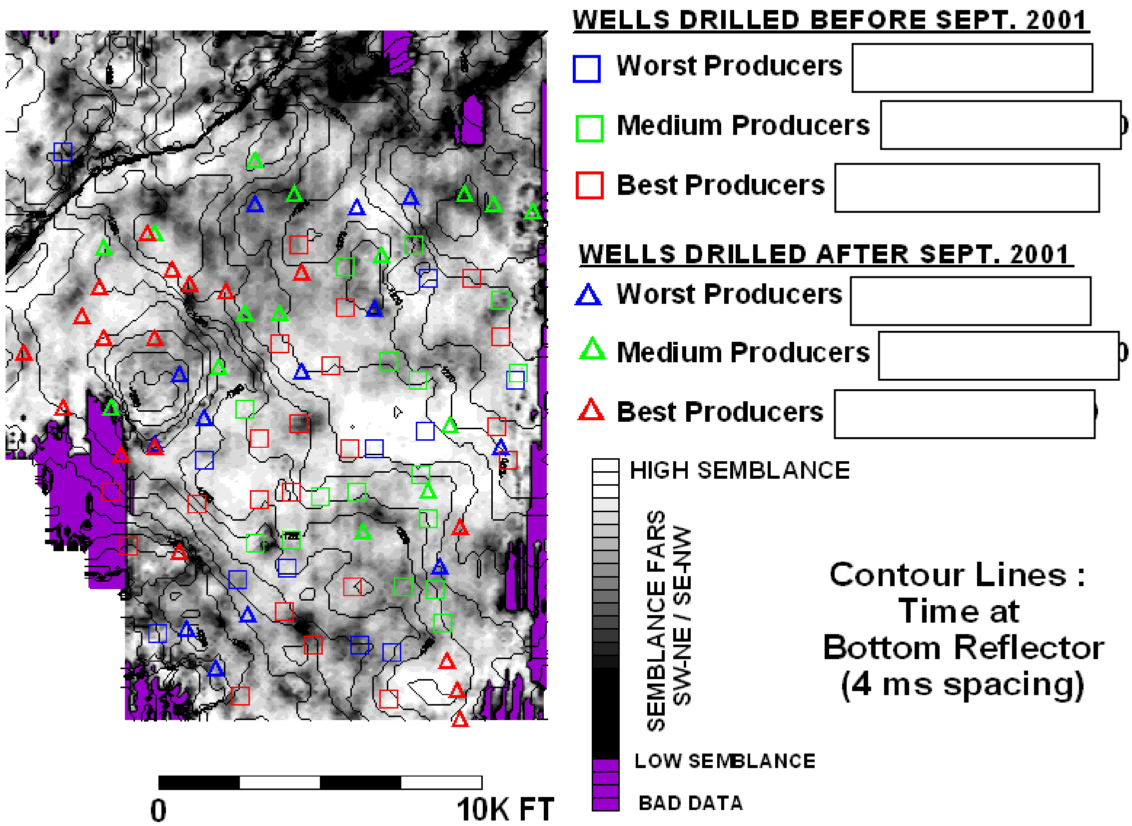

Figure 39: E.U.R. of all wells and inter-azimuth similarity, far offset.

7.4. Discussion of the inter-azimuth similarity results

The normalized correlations found, and the examination of the maps, are disappointing. It seems that the inter-azimuth attribute cannot be used to predict gas production in this field, despite the fact that the maps show linear features aligned SW-NE or SE-NW, as expected.

Nevertheless, I believe that this new attribute could be useful in other reservoirs, more dependent on natural vertical aligned fractures instead of dominant horizontal stress.

Usage of only two azimuths is another reason for the disappointing results. Ideally, the data should be subdivided into 4 or 8 azimuths. Then, a search should be made to find which pair of orthogonal azimuths shows the greatest dissimilarity. This requires high-fold data, to preserve a sufficient signal to noise.

8. COMBINATIONS OF SEISMIC ATTRIBUTES

The presence of spurious values along the edges of the survey has a very strong biasing effect on the results when comparing seismic attributes; therefore, I cropped the survey to remove less reliable values, and kept approximately half of the total area, south of the main fault.

8.1. Curvature of top and bottom reflector

I began by crossplotting K+ on the bottom reflector and K+ on the top reflector. I obtained a high correlation, $\rho = 0.69$ (Figure 39), that verifies that curvature within the reservoir is due to post-genesis horizontal stress, and was not pre-existent to the deposition of shale. Indeed, any pre-existing curvature of the bottom reflector would have been strongly attenuated at the top level by differential filling with shale. I did the same with K-, and as expected, I also observe a high correlation, $\rho = 0.68$ (Figure 40).

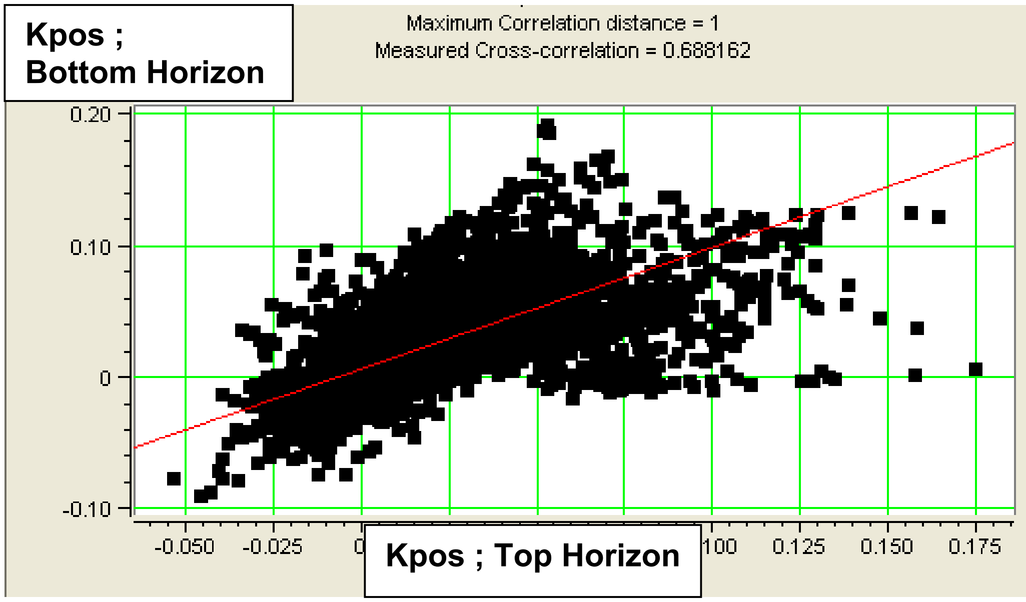

Figure 40: Most positive curvature (K+) of bottom reflector versus K+ of top reflector; excellent correlation, ρ = 0.69

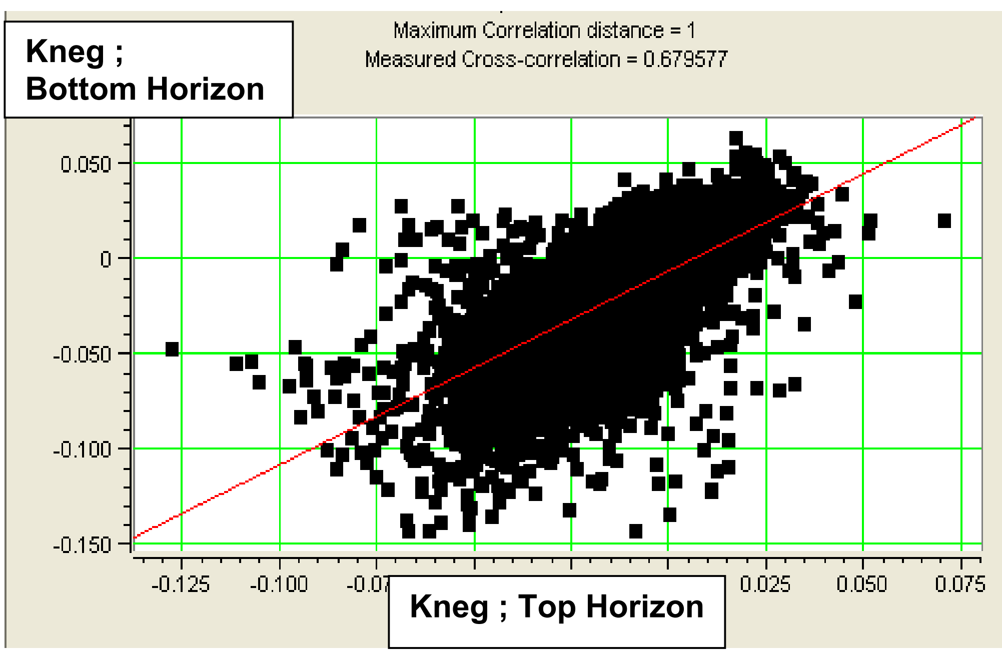

Figure 41: Most negative curvature (K-) of the bottom reflector versus K- of top reflector; excellent correlation, ρ = 0.68

8.2. Azimuthal interval velocity and curvature

I assume that curvature due to post-genesis stress creates multi-azimuth fractures and multi-azimuth stress relief. Therefore, I crossplotted the absolute value of Kmax versus Vfast in the middle of the reservoir. If my assumption is correct, I should find an inverse correlation. Unfortunately, with | Kmax | on the bottom reflector, I found a ρ of only 0.11, and on the top reflector, $\rho = -0.01$. This can be due to the fact that, in many instances, curvatures creates a dominant horizontal stress field in one azimuth, or that horizontal stress and vertical fractures are due to other causes than curvature.

Then, I overlaid arrows (azimuthal interval velocity attributes) on:

- Maximum curvature (Kmax) of the bottom reflector (Figure 42)

- Maximum curvature (Kmax) of the top reflector (Figure 44)

A striking observation, highlighted by Figure 43 (which is a detail of Figure 42), is that the azimuth of Vfast is parallel to the azimuth of linear positive (convex) Kmax areas.

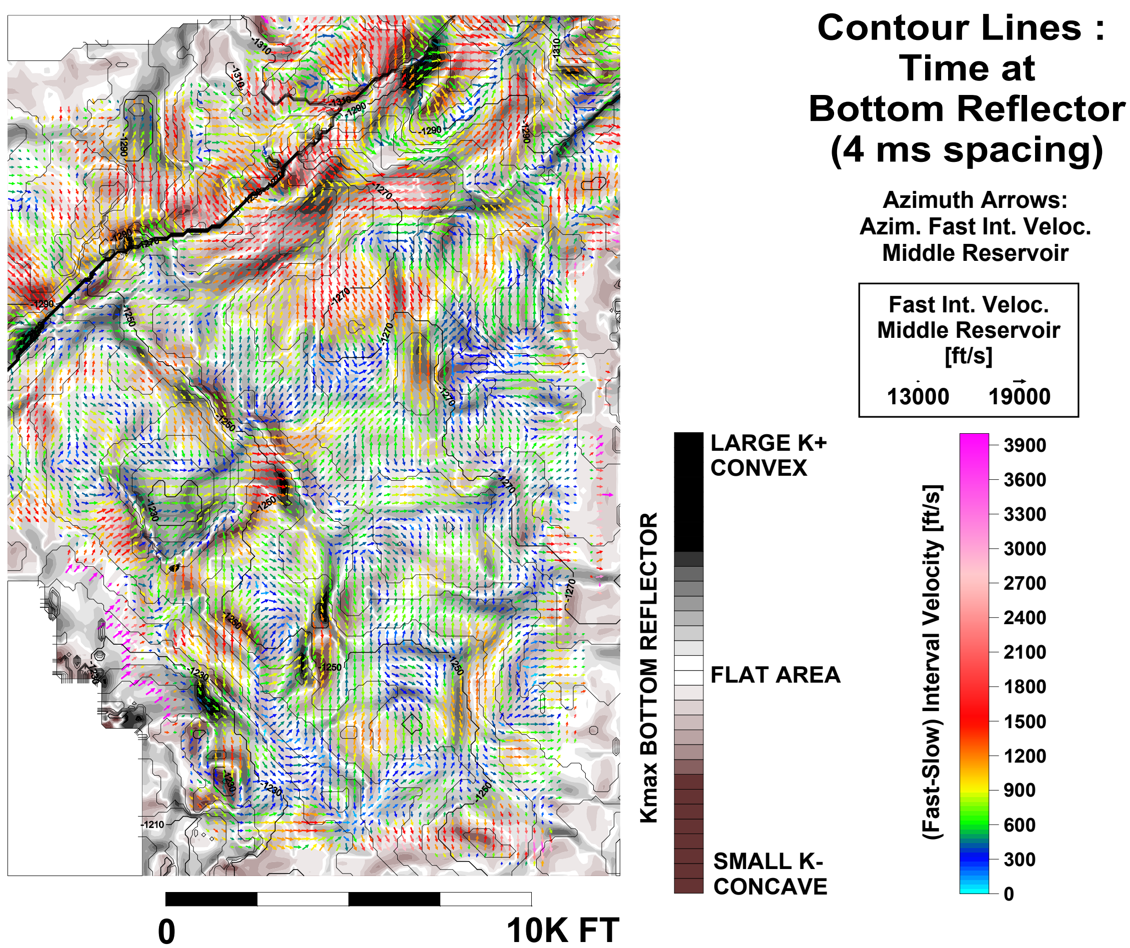

Figure 42: Background color: Kmax of bottom reflector. Arrows: interval velocity attributes (size is Vfast, colors are Vf-Vs, Azimuth is azimuth of Vfast)

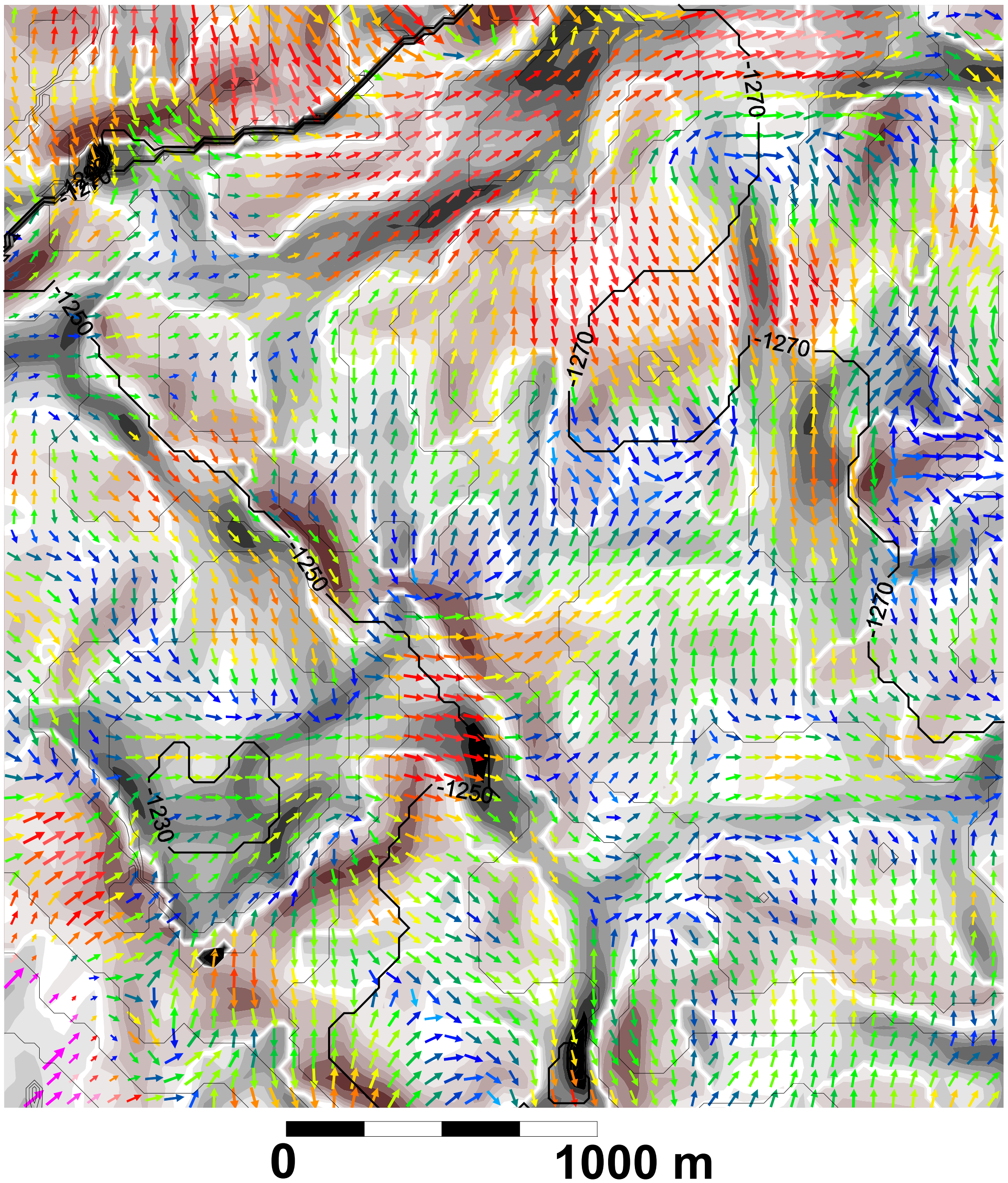

Figure 43: Detail of Figure 42, color scales are the same. Azimuth of arrows (Vfast) similar to linear gray areas (ridges)

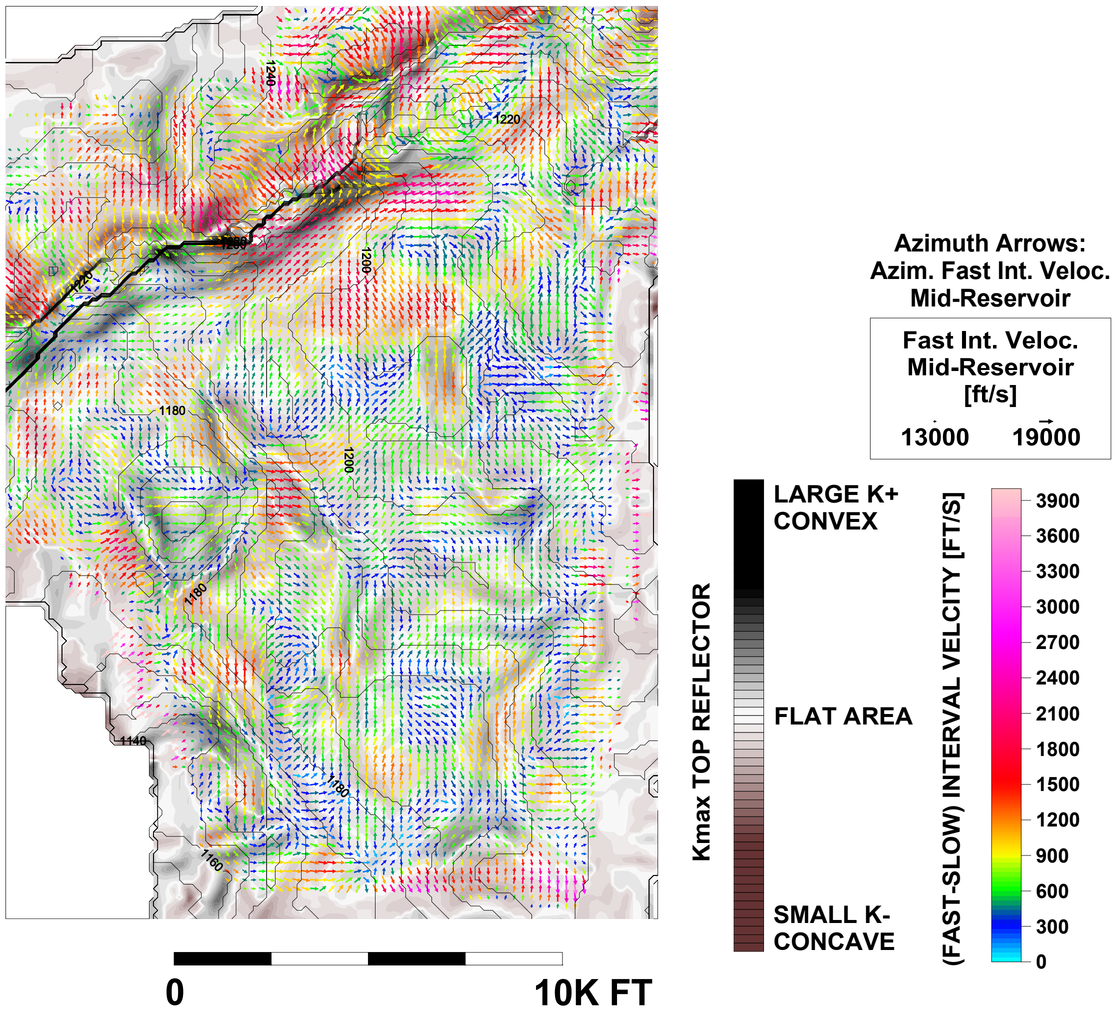

Figure 44: Color-filled contours (Kmax of top reflector),overlaid by arrows (interval velocity attributes: size is linked with Vfast, colors show Vf-Vs, azimuth is azimuth of Vfast)

8.3. Azimuthal interval velocity attributes and inter-azimuth similarity

In the middle of the shale reservoir, I crossplotted the inter-azimuth similarity between the Nears (80 ms vertical window) and [(Vf-Vs)/Vf]. The correlation is very small, ρ = -0.07. Both measurements are a measurement of azimuthal anisotropy within the reservoir, and this poor result was unexpected.

I repeated the process with the inter-azimuth similarity of the Fars and [(Vf-Vs)/Vf]. Again, the normalized cross-correlation, although better, is poor, ρ = -0.23.

The fast interval velocity and the similarity of the Nears in the middle of the reservoir show a small inverse correlation, ρ = -0.15. But the fast interval velocity versus the similarity of the Fars in the middle of the reservoir shows a very significant inverse correlation, ρ -0.46 (Figure 45).

These results are difficult to interpret, and to try to understand them better, I made multi-layer maps:

- Similarity SW-NE / SE-NW Nears, bottom horizon, ±10 ms overlaid by arrows displaying azimuthal interval velocity attributes (Figure 46).

- Similarity SW-NE / SE-NW Fars, bottom horizon, ±10 ms overlaid by arrows displaying azimuthal interval velocity attributes (Figure 47).

These maps confirm my numerical correlations, but do not help to explain why there is a strong inverse correlation between the similarity of the Fars and Vfast in the middle of the reservoir.

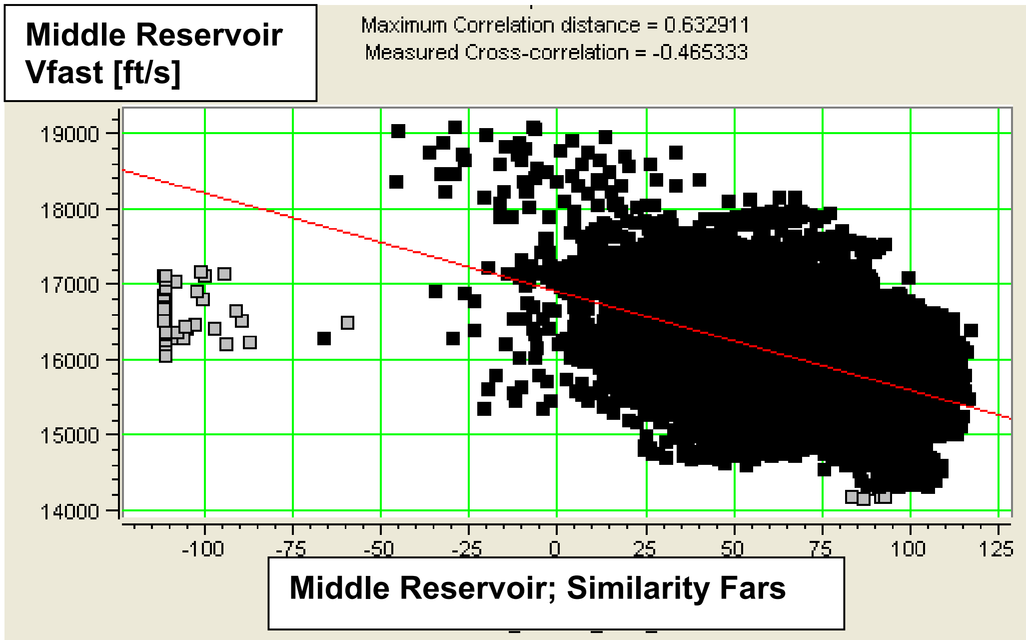

Figure 45: Middle of the reservoir: Inter-azimuth similarity, Far offset, 80ms vertical window versus Vfast, cropped area. ρ = -0.48

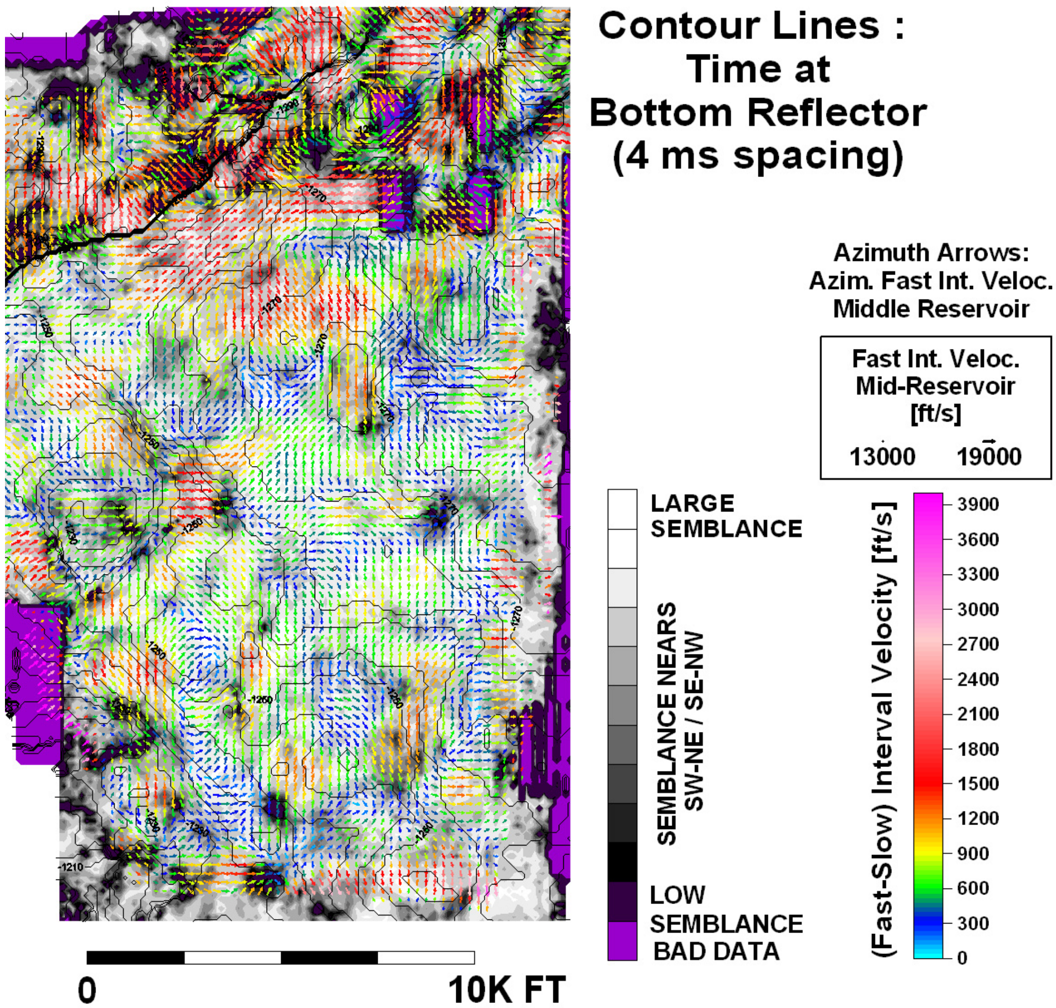

Figure 46: Color-filled contours (Similarity Nears, Bottom reflector, 20ms windows),overlaid by arrows (interval velocity attributes: size is linked with Vfast, colors show Vf-Vs, azimuth is azimuth of Vfast)

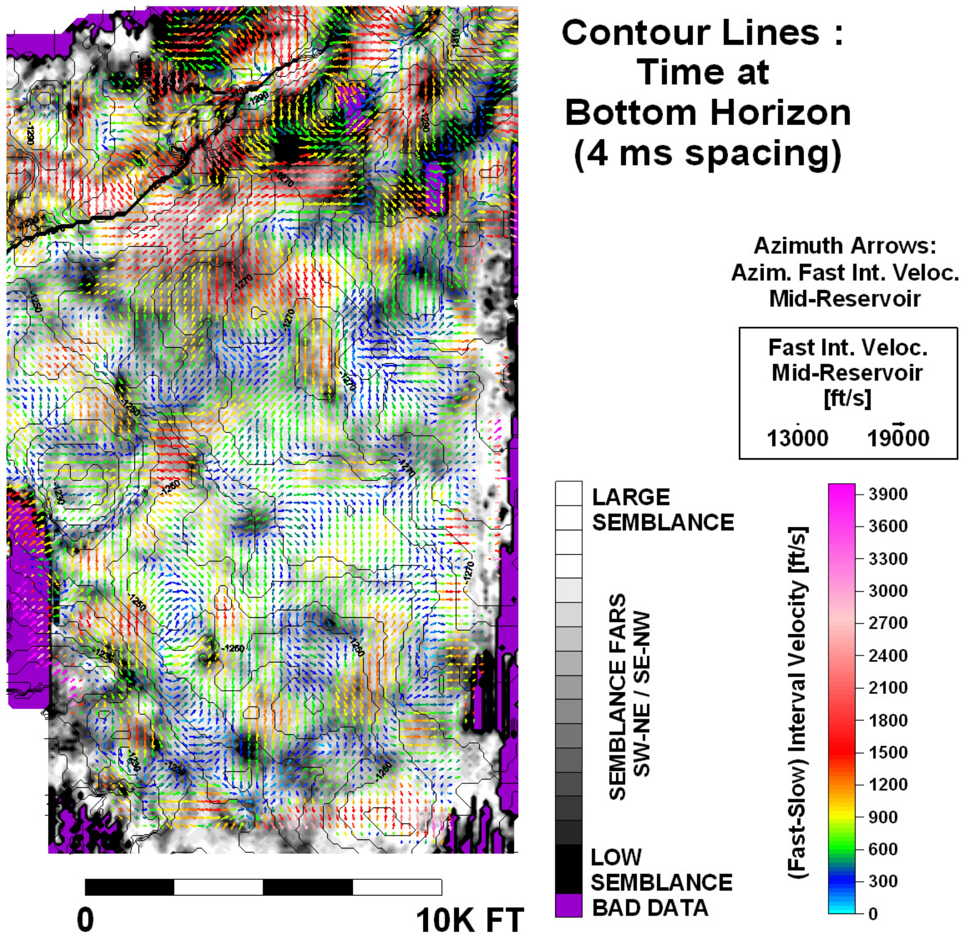

Figure 47: Color-filled contours (Similarity Fars, Bottom reflector, 20ms window), overlaid by arrows (interval velocity attributes: size is linked with Vfast, colors show Vf-Vs, azimuth is azimuth of Vfast)

8.4. Inter-azimuth Similarity: Nears versus Fars

At the bottom reflector level, using a 20 ms window, I compared the similarity between the NE-SW traces and SW-NE traces for the Nears (0°-20°) and the Fars (20°-45°). I obtained a ρ of 0.54 (Figure 48). This result is surprisingly high, as it is commonly thought that the Fars are more sensitive to vertical aligned fractures and horizontal stress due to a larger angle of incidence. But this assumption is highly controversial, as confirmed by Heloise Lynn (personal communication, July 2005). Indeed, compared to the Fars, the Nears are less exposed to anisotropy in the overburden, since the travelpath is shorter. Another point to keep in mind is that, in this field, azimuthal anisotropy is essentially due to differential horizontal stress, not due to the presence of fractures. It is possible that near-offset P-waves are more able to detect azimuthal stress than vertical aligned fractures.

The same analysis was done at the top reflector. The correlation is lower ($\rho = 0.31$), but still significant. The difference is probably due to the presence of a second reflector (a trough) within the vertical window (20 ms) used, degrading the results.

I did compare histograms of similarity between Nears and between Fars. As expected, there are more low values (less similarity between traces) for the Fars.

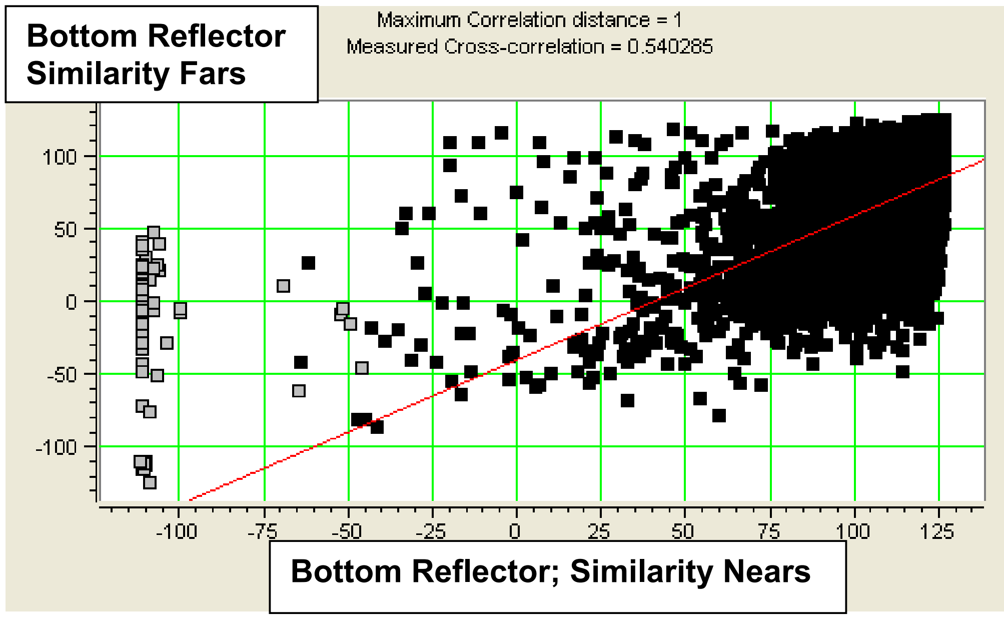

Figure 48: Bottom Reflector; 20ms Vertical window; Similarity Nears versus similarity Fars; $\rho = 0.54$

9. CONCLUSIONS

This work examined many new seismic attributes, independently and in combinations, to determine correlation with gas production, which depends mainly on azimuth of dominant horizontal stress and possibly natural fracture density and azimuth, in a North Texas shale reservoir. Many insights were gained by this work.

Only one seismic attribute shows a significant correlation with E.U.R. using crossplots: the fast interval velocity.

Nevertheless, an excellent visual correlation between induced fractures mapped by microseismic experiment and azimuthal interval velocity attributes was observed on multi layer maps: creation of SE-NW induced fractures by hydrofracs is associated with a combination of medium to high velocity anisotropy, and SE-NW azimuth of Vfast.

The stress field around the wells is modified by hydrofracs, as shown by the difference of ρ between Vfast and the E.U.R. of the wells drilled and hydrofrac'd before or after the 3D seismic acquisition, and by the good visual correlation between azimuthal interval velocity and induced fractures mapped by microseismic measurement around two wells drilled after the 3D seismic acquisition, in contrast with the absence of visual correlation around wells drilled before the 3D seismic acquisition.

The high degree of correlation between the curvature of the bottom and the top reflector of the reservoir is consistent with the effect of post-genesis horizontal stress. I can cautiously infer that curvature should be a good indicator of changes in the local horizontal stress field and presence of vertical fractures.

Crossplots of azimuthal interval velocity attributes and curvature attributes have shown poor linear correlations. However, visual examination of the map of Kmax overlaid by icons representing azimuthal interval velocity attributes, shows that the azimuth of Vfast in the reservoir is similar to the azimuth of linear, convex areas (“ridges”) on the bottom reflector. I interpret this to mean that the reservoir is above the neutral plane of these ridges, and that the azimuth of the local horizontal stress field and possibly vertical fractures is similar to the azimuth of the ridges.

For one well monitored by microseismic measurements, the map of Kmax at the top reflector of the reservoir shows a correlation with induced fractures. This is an incentive to search for more efficient ways to use curvature attributes to define horizontal stress and vertical fractures, taking into account the low cost of these attributes and their independence from modification of the local stress field by hydrofrac'd wells.

Despite an average similarity higher for the Nears than the Fars, the inter-azimuth similarity of the Nears (offset of 0° to 20° at target depth) is highly correlated to the inter-azimuth similarity of the Fars (offset larger than 20° at target depth). This result goes against the general belief that only the far offsets are sensitive to azimuthal velocity anisotropy. One possible explanation is that, in this field, dominant horizontal stress azimuth is the more important factor regarding azimuthal anisotropy, not aligned vertical fractures. The capacity of the Nears to detect the dominant horizontal stress implies that, for similar fields, our inter-azimuth similarity attribute can be used with narrower 3D seismic surveys, more common and less expensive to acquire and process.

Histograms and linear numerical correlations are limited tools. They cannot replace visual examination of multi layer attribute maps by a skilled interpreter, and should be considered only as additional tools.

10. REFERENCES

Al-Dossary, S., Y. S. Simon and K. J. Marfurt, 2004, Inter azimuth coherence attribute for fracture detection: SEG, 74th Annual International Meeting Expanded Abstracts, **23**, 183.

Bourne, S. J.., F. Brauckman, L. Rijkels, B. J. Stephenson, A. Weber and E. J.M. Willemse, 2000, Predictive modeling of naturally fractured reservoirs using geomechanics and flow simulation: 9th Abu Dhabi International Petroleum Exhibition and Conference (ADIPEC), 0911.

Fisher, M. K., C.A. Wright, B. M. Davidson, E. O. Fielder, W. S. Buckler and N. P. Steinsberger, 2003, Integrating Fracture Mapping Technologies to Optimize Simulations in the Barnett Shale: Society of Petroleum Engineers, SPE 77441.

Flawn, P. T., A. Goldstein Jr., P. B. King, and C. E. Weaver, 1961, The Ouachita System: University of Texas at Austin, Bureau of Economic Geology, Publication 6120, 401 p.

Grechka, V. and I. Tsvankin, 1998, 3-D description of normal-moveout in anisotropic inhomogeneous media, Geophysics, **63**, 1079-1092

Grechka, V., I. Tsvankin and J. K. Cohen, 1999, Generalized Dix equation and analytic treatment of normal-moveout velocity for anisotropic media, Geophysical Propecting, **47,** 117-148

Heidelberg Academy of Sciences, 1999, World Stress Map.

Jenner, E., 2001, Azimuthal Anisotropy of 3-D Compressional Wave Seismic Data, Weyburn Field, Saskatchewan, Canada: PhD thesis, Colorado School of Mines.

Lancaster, D. E., S. F. McKetta, R. E. Hill, F. K. Guidry and J. E. Jochen, 1992, Reservoir Evaluation, Completion Techniques, and Recent Results from Barnett Shale Development in the Fort Worth Basin: Society of Petroleum Engineers, SPE 24884.

Landes, K. K., 1970, Petroleum Geology of the United States: Chapter 29 (North Texas), John Wiley & Sons, 294-307.

Lynn, H. B., and Y. S. Simon, 2002, Co-rendering and Interpretation of nine 3D-attribute volumes, Denver Geophysical Society, Technical Luncheon, November 14th.

Lynn, H. B., 2004, The Winds of Change, Anisotropic rocks – their preferred direction of fluid flow and their associated seismic signatures – Part 1 and Part 2: The Leading Edge, **23**, 1156-1162 and 1258-1268.

Montgomery, S. L., D. M. Jarvie, K. A. Bowker, and R. M. Pollastro, 2005, Mississippian Barnett Shale, Fort Worth Basin, north-central Texas: Gas-shale play with multi-trillion cubic foot potential: AAPG Bulletin, **89**, 155-175.

Nissen, S. E., R. C. Thimothy, K. J. Marfurt, 2004, Using New 3-D Seismic Attributes to Identify Subtle Fracture Trends in Mid-Continent Mississippian Carbonate Reservoirs: Kansas Geological Survey, **56**.

Pollastro, R. M., R. J. Hill, D. M. Jarvie, M. E. Henry, 2003, Assessing Undiscovered Resources of the Barnett-Paleozoic Total Petroleum System, Bend Arch-Fort Worth Basin Province, Texas: AAPG Southwest Section Meeting, Fort Worth, Texas, March.

Roberts, A., 2001, Curvature attributes and their application to 3D interpreted horizons: First Break, 19.2.

Stearns, D.W., and M. Friedman, 1972, Reservoirs in fractured rock, *in* King, R.E., editor, Stratigraphic oil and gas fields - classification, exploration methods, and case histories: American Association of Petroleum Geologists Memoir **16**, 82-106.

Thompson, D. M., 1982, Atoka Group, Northern Fort Worth Basin, Texas: Terrigenous Depositional Systems, Diagenesis, and Reservoir Distribution and Quality: Bureau of Economic Geology, Report of Investigations, **125.**

Walper, J. L., 1982, Plate tectonic evolution of the Fort Worth basin, in Martin, C. A., ed., Petroleum Geology of the Fort Worth basin and Bend Arch area, Dallas Geological Society, 237-251.

Williams, M., and E. Jenner, 2002, Interpreting seismic data in the presence of azimuthal anisotropy; or azimuthal anisotropy in the presence of the seismic interpretation: The Leading Edge, **21,** 771-774.

APPENDIX A: FUTURE WORK

Based on this study, I have listed below interesting additional work that could be done to improve the correlations, and therefore to predict best locations for new wells:

- Deletion of the values of Vf-Vs and azimuth of Vf when the error estimation of the ellipse fitting is high. After looking at the error estimation maps, it seems that it can only make a small difference for this specific reservoir, the degree of error being small. It is a lot more important for amplitude-based attributes.

- Numerical correlation between azimuth of Kmin and E.U.R.s when (Kmax – Kmin) is large. The best way to do this requires a cosine ($2\ \theta$) curve fitting, because the azimuth of Vfast goes from 0° to 180°. This scale is circular, not linear. But it can be done, too, by dividing the wells into groups defined by a range of Kmin azimuth. In this study, a similar method was used successfully with the azimuthal interval velocity attributes.

- To know that we are in a convex or in a concave area, by itself, does not tell us the azimuth of stress relief, nor the azimuth of fracturing. It depends on the depth too, and if we are above or below the neutral plane of the curved volume. For example, above a linear convex area on a reflector, the largest horizontal stress will be parallel to the lineament if we are above the neutral plane, but orthogonal if we are below the neutral plane. Therefore, we could try to estimate where a curve begins and ends (in depth), by examination of many surfaces at different depths.

- To distinguish between curvature of the reservoir due to post-genesis bending (good indication of stress relief / presence of fractures) and pre-existing curvature filled by depositional process of shale, areas where Kmax is large (convex area) or small (concave area), and the difference between Kmax at the bottom and the top of the reservoir is small, can be selected. The improvement will probably be small, due to the excellent cross-correlation obtained between curvature on the top and the bottom of the reservoir;

- To compare the interval velocity anisotropy [(Vf-Vs) / Vf] with the inter-azimuth semblance attribute, we could ignore the values when the azimuth of Vf is not between 22.5° and 67.5° or between 112.5° and 157.5°. Indeed, horizontal stress and / or fractures cannot be detected by inter-azimuth semblance between SW-NE and SE-NW volumes outside these ranges of azimuth. The result would show if the azimuthal anisotropy of interval velocity is sensitive to the same geological features than the inter-azimuth similarity of traces;

- Creation of combination of attributes maps to pinpoint the most prospective locations.

APPENDIX B: TABLE OF EXTRACTED SEISMIC ATTRIBUTES

ATTRIBUTE	ABBREV.	LEVEL	LEVEL	LEVEL	LEVEL
Azimuth of Fastest Int. Velocity	AzimVfast	x	x	Mid-Reservoir	x
Fastest Interval Velocity	Vfast	x	x	Mid-Reservoir	x
Fastest - Slowest Int. Velocity	Vfast - Vslow	x	x	Mid-Reservoir	x
Maximum Curvature	Kmax	Bot	x	x	Top
Positive Curvature	K+	Bot	x	x	Top
Negative Curvature	K-	Bot	x	x	Top
Simil. Near Offsets, 20ms Win	SimNears±10	Bot	Bot-6ms	Bot-20ms	Top+6ms
Simil. Far Offsets, 20ms Win	SimFars±10	Bot	Bot-6ms	Bot-20ms	Top+6ms
Simil. Near Offsets, 80 ms Win	SimNears40	Bot-10ms	Bot-35ms	Mid-Reservoir	Top+10ms
Simil. Far Offsets, 80 ms Win	SimFars40	Bot-10ms	Bot-35ms	Mid-Reservoir	Top+10ms

APPENDIX C: MAIN PROGRAMS USED

Corel Quattro Pro: Spreadsheet

Golden Software Grapher: Graphics.

Golden Software Strater: Well log displays.

Golden Software Surfer: Maps.

Hampson-Russell ISmap: Geostatistics.

Microsoft Excel: Spreadsheet.

Microsoft PowerPoint: Figures and slides.

Microsoft Word: Word processor.

Schlumberger Geoquest IESX: 3D seismic interpretation.

Ulead PhotoImpact: Image editing.

Vest Exploration 3Dseis: 3D seismic interpretation.

APPENDIX D: ADDITIONAL READING

Fort Worth Basin / Shale reservoirs

Bowker, K., 2004, The Barnett Shale Gas Play, Fort Worth Basin: HGS North American Explorationists Dinner, January 26th.

Burstin, M. R., 2005, Gas Shale Tapped for Big Pay: AAPG Explorer, February.

Curtis, J. B., 2002, Fractured shale-gas systems: AAPG Bulletin, **86**, 1921-1938.

Fisher, M. K., J. R. Heinze, C. D. Harris, B. M. Davidson, C. A. Wright and K. P. Dunn, 2004, Optimizing Horizontal Completion Techniques in the Barnett Shale Using Microseismic Fracture Mapping: Society of Petroleum Engineers, SPE 90051.

Hills, D. G., and C. R. Nelson, 2000, Gas Productive Fractures Shales: an Overview and Update: Gas TIPS, Summer 2000.

Johnston, D., 2004, Technological advances expand potential pay – Barnett Shale: Oil & Gas Journal, January 19.

Maxwell, S. C., T. I. Urbancic, N. Steinsberger and R. Zinno, 2002, Microseismic Imaging of Hydraulic Fracture Complexity in the Barnett Shale: Society of Petroleum Engineers, SPE 77440.

Shirley, K., 2002, Infrastructure Key to Gas Play: Barnett Shale Living Up to Potential: Explorer, July 2002.

Azimuthal Anisotropy (HTI)

Al-Marzoug, A. M., F. A. Neves, J. J. Kim, E. L. Nebrija, 2004, P-wave Anisotropy from Azimuthal Velocity and AVO using Wide-Azimuth 3D Seismic Data: SEG, 74th Annual International Meeting, Expanded Abstracts, **23,** 131-134.

Bates, C. R., H. B. Lynn, and K. M. Simon, 1999, The Study of a Naturally Fractured Gas Reservoir Using Seismic Techniques: AAPG Bulletin, **83**, 1392-1407.

Bates, C. R., D. R. Phillips, R. Grimm, and H. B. Lynn, 2001, The seismic evaluation of a naturally fractured tight gas sand reservoir in the Wind River Basin, Wyoming: Petroleum Geoscience, **7,** 35-44.

Crampin, S., 1985, Evaluation of anisotropy by shear-wave splitting: Geophysics, **50**, 142-152.

Gomez, C. and E. Angerer, 2004, Wide-Azimuth processing for azimuthal anisotropy analysis: SEG, 74th Annual International Meeting, Expanded Abstracts, **23,** 167-170.

Gray, D., G. Roberts, and K. Head, 2002, Recent advances in determination of fracture strike and crack density from P-wave seismic data: The Leading Edge, **21**, 280-285.

Grimm, R. E., H. B. Lynn, C. R. Bates, D. V. Phillips, K. M. Simon and W. E. Beckham, 1999, Detection and analysis of naturally fractured gas reservoir: Multiazimuth seismic surveys in the Wind River basin, Wyoming: Geophysics, **64**, 1277-1292.

Jenner, E., 2002, Azimuthal AVO Methodology and data examples: The Leading Edge, **21**, 782-786.

Li, X.-Y., 1999, Fracture detection using azimuthal variation of P-wave moveout from orthogonal seismic survey lines: Geophysics, **64,** 1193-1201.

Lynn, H. B., K. M. Simon, R. C. Bates and R. Van Dok, 1996, Azimuthal anisotropy in P-wave 3-D (multiazimuth) data: The Leading Edge, **15,** August.

Lynn, H. B., K. M. Simon, and C. R. Bates, 1996, Correlation between P-wave AVOA and S-wave traveltime anisotropy in a naturally fractured gas reservoir: The Leading Edge, **15**, 931–935.

Lynn, H. B., D. Campagna, K. M. Simon, and W. Beckham, 1999, Relationship of P-wave seismic attributes, azimuthal anisotropy, and commercial gas pay in 3-D P-wave multiazimuth data, Rulison field, Piceance Basin, Colorado: Geophysics, **64,** 1293.

Lynn, H. B., W. B. Beckham, K. M. Simon, C. R. Bates, M. Layman, M. Jones, 1999, P-wave and S-wave azimuthal anisotropy at a naturally fractured gas reservoir, Bluebell-Altamont Field, Utah: Geophysics, **64**, 1312-1328.

Mallick, S., K. L. Craft, L. J. Meister, and R. E. Chambers, 1996, Computation of principal directions of azimuthal anisotropy from P-wave seismic data: 66th Annual International Meeting, SEG, Expanded Abstracts, **15,** 1862-1865.

Neves, F. A., A. K. Al-Marzoug, J. Jung, and E. L. Nebrija, 2003, Fracture characterization of deep tight gas sands using azimuthal velocity and AVO seismic data in Saudi Arabia: The Leading Edge, **22**, 469-475.

Ruger, A., 2002, Reflection Coefficients and Azimuthal AVO Analysis in Anisotropic Media: SEG, Geophysical monograph series, **10.**

Thomsen, L., 2002, Understanding Seismic Anisotropy in Exploration and Exploitation: SEG, Distinguished Instructor Series, **5.**

Xiaoxia, X. and I. Tsvankin, 2004, Geometrical-spreading correction for P-waves in layered azimuthally anisotropic media: SEG, 74th Annual International Meeting, Expanded Abstracts, 23, 111.

Other Seismic Attributes for fractures and stress detection

Bahorich, M. S., and S. L. Farmer, 1995, 3-D seismic discontinuity for faults and stratigraphic features: The coherence cube: The Leading Edge, **14,** 1053-1058.

Chopra, S., V. Sudhakar, G. Larsen, and H. Leong, 2000, Azimuth-based coherence for detecting faults and fractures: World Oil Magazine, **221,** September.

Dalley, R. M., E. E. A. Gevers, G. M. Stampli, D. J. Davies, C. N. Gastaldi, P. R. Ruijetnberg, and G. J. D. Vermeer, 1989, Dip and azimuth displays for 3-D seismic interpretation: First Break, **7**, 86-95.

Hakami, A. H., K. J. Marfurt and S. Al-Dossary, 2004, Curvature Attribute and seismic interpretation: Case study from Fort Worth Basin, Texas, USA: SEG, 74th Annual International Meeting , Expanded Abstracts, **23,** 544.

Marfurt, K. J., R. L. Kirlin, S. L. Farmer, and M. S. Bahorich, 1998, 3-D seismic attributes using a semblance-based coherency algorithm: Geophysics, **63**, 1150-1165.

Neves, F. A., M. S. Zahrani, and S. W. Bremkamp, 2004, Detection of potential fractures and small faults using seismic attributes: The Leading Edge, **23,** 903-906.

Geostatistics

Dubrule, O., 2003, Geostatistics for Seismic Data Integration in Earth Models: SEG, Distinguished Instructor Series, **6.**

Russell, B. H., D. Hampson, and T. Todorov, 2001, Combining geostatistics and multiattribute transforms - A channel sand case study: SEG, 71st Annual International Meeting, Expanded Abstracts, **20.**